

Room-Temperature Ballistic Nanodevices

Aimin M. Song

Department of Electrical Engineering and Electronics, University of Manchester Institute of Science and Technology, Manchester M60 1QD, England

CONTENTS

1. Introduction
 2. Ballistic Rectifiers and Semiclassical Model
 3. Artificial Functional Nanomaterials
 4. Three-Terminal Ballistic Junction Devices
 5. Near Room-Temperature Operations of Quantum-Effect-Based Devices
 6. Conclusions and Outlook
- Glossary
Acknowledgments
References

1. INTRODUCTION

One of the most important physical parameters to describe the quality of a piece of semiconductor material is the electron scattering length l_e . Also referred to as the mean-free path, it stands for the average distance between the randomly distributed scatterers in the material, such as lattice defects, impurities, and phonons. The electron mean-free path is typically a few nanometers ($1 \text{ nm} = 10^{-9} \text{ m}$) in silicon and about 100–200 nm in high-quality compound semiconductors such as GaAs. The electrical resistance of a semiconductor device is closely associated with the scattering length l_e . Conventional semiconductor devices are much larger than the electron scattering length. As a result, electrons have to encounter a large number of random scattering events to travel from one device lead to another. In the last two decades, advanced semiconductor technologies have allowed the fabrication of devices that are smaller than the electron scattering length. In such devices, electrons may travel from one electric lead to another without encountering any scattering event from randomly distributed scatterers such as impurities. Instead, the electrons are scattered only at the device boundaries, that is, moving like billiard balls. Such electron transport is referred to as ballistic transport [1–3]. There had been a long debate in history on whether there is any electric resistance in such ballistic electron devices. Some had believed that the absence of

scattering means that the resistivity inside the device is zero. Although this is, as will be discussed later, wrong because the concept of resistivity does not hold any longer in the ballistic transport regime, it was realized quite clearly that the electron transport in a ballistic device is very different from the transport in a traditional, macroscopic semiconductor device.

Consider a conventional semiconductor device that is much larger than the electron scattering length. Any electric current induced by an applied voltage consists of electrons diffusing in an electric field, as shown in Figure 1. The diffusive transport can be described by Ohm's law, which states a linear relation between the current and electric field (or applied voltage). However, if we examine the electron transport at the microscopic scale, we would find that every electron is accelerated between two subsequent scattering events by the electric field. As a result, the velocity component of the electron in the opposite direction of the electric field increases constantly until the next scattering event occurs. Since the current carried by the electron is equal to its velocity multiplied by the electron charge e , the current is time dependent, even in the presence of a constant electric field. This is seemingly in contradiction to Ohm's law. Actually, Ohm's law is valid at the macroscopic scale because of the existence of the large number of scattering events, which counteract the acceleration effect of the electric field, causing the average velocity of all electrons to be proportional to the strength of the electric field. The above discussion reveals that, at a scale that is smaller than the average distance between impurities or other scatterers, Ohm's law does not hold, and that new transport properties are expected to arise in these ballistic devices of a dimension smaller than l_e .

A number of new device concepts have been generated based on ballistic electron transport in the last two decades. Among these novel devices are only a few that have been demonstrated to work at room temperature. Quite understandably, being capable of operating at room temperature is an important criterion for practical applications. In this chapter, we review these recent breakthroughs in room-temperature ballistic devices. The theoretical framework to treat ballistic electron transport, namely, the scattering

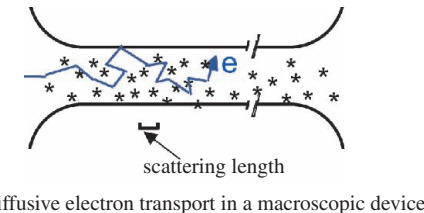


Figure 1. Schematic view of the diffusive electron transport in a macroscopic semiconductor device. The device size is much larger than the electron scattering length. As a result, the electrons experience a large number of scattering events from randomly distributed scatterers such as lattice defects and phonons (represented by the asterisks), and the electron transport is hence referred to as diffusive.

approach developed by Landauer and Büttiker, will be introduced. We will also discuss the promising possibilities for practical applications of these devices from the point of view of their new device properties. The chapter is organized as follows. After a short introduction to the ballistic transport in Section 1.1, an overview of the general aspects of nonlinear ballistic electron transport is presented in Section 1.2, which forms a basis for the few types of room-temperature nanodevices and nanomaterials discussed in Sections 2–4. In Section 5, promising results on near room-temperature operations of quantum-effect-based nanodevices are discussed. Finally, Section 6 provides conclusions and an outlook of future developments.

1.1. Overview of Ballistic Electron Transport

Ballistic electron transport is normally realized in mesoscopic semiconductor structures. The word “mesoscopic” refers to dimensions between the atomic scale and the macroscopic scale. The simplest mesoscopic ballistic device is a narrow, uniform semiconductor channel, as shown in Figure 2. At a finite applied voltage, a current flows through the channel. If the length of the channel is shorter than l_e , the electron transport inside the channel is ballistic. The electrons, when moving from one side of the channel to the other, do not experience any random scattering event from scatterers such as lattice defects, impurities, and phonons, but are scattered only by the designed device boundary. This

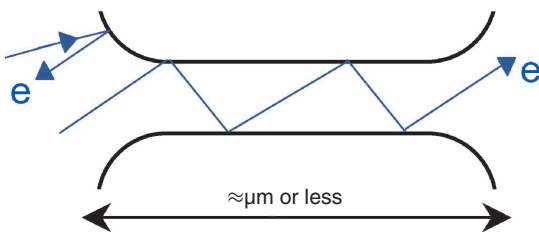


Figure 2. Schematic view of the ballistic electron transport in a mesoscopic semiconductor device, which is smaller than the electron scattering length. In the device, the electrons do not experience any scattering event from random scatterers such as lattice defects and phonons, and are only scattered by the designed device boundary.

means that, even at a finite applied voltage, the electric field, and therefore the voltage drop inside the central part of the channel, which has a constant width, have to be zero in order to fulfill the requirement of the conservation of current: the current flow into one end of the channel must be the same as the current flow out of the channel at the other end. Therefore, inside the channel, current flows without the existence of a finite electric field. The striking phenomenon appears to be similar to the superconductivity effect, but occurring in a completely different physics system under a different physical condition. Such an effect of current flow without the presence of an electric field has been observed regardless of the length and width of the channel, as long as the channel is shorter than the electron mean-free path. Nevertheless, to drive a current through the entire device, a finite voltage has to be applied. The applied voltage will only drop at the entrance and exit of the channel, where finite resistance arises because most of the electrons are backscattered and only a fraction of the electrons can enter the channel [4]. As a consequence, the electric field exists only in the close vicinity of the entrance and exit of the channel. Clearly, local quantities such as resistivity and conductivity lose their meaning, and can no longer be defined in a ballistic semiconductor device. Only nonlocal quantities such as the total resistance or conductance can be used.

The conductance of a ballistic semiconductor device G is determined by an important nonlocal quantity: the transmission coefficient $T_{\beta \leftarrow \alpha}$ of the ballistic electrons going from one electric contact (also often referred to as the electric lead, carrier reservoir, or device terminal) α to another contact β . If more than one transverse quantum confinement mode in the device is occupied, $T_{\beta \leftarrow \alpha}$ is the sum of the transmission probabilities of the electrons at each occupied transverse quantum confinement mode i :

$$T_{\beta \leftarrow \alpha} = \sum_i t_{\beta \leftarrow \alpha, i} \quad (1)$$

As described by the Landauer–Büttiker formula [5–7], the current flow through the narrow channel is given by

$$I = \frac{2e}{h} \sum_i t_{\beta \leftarrow \alpha, i} (\mu_\alpha - \mu_\beta) \quad (2)$$

where μ_α and μ_β are the chemical potentials of the electrons at the left and right contacts of the channel. If the electrons at each transverse mode transfer through the channel perfectly (without being reflected back), which was found to be the case if the boundary of a narrow channel is smooth and if the temperature is sufficiently low [8, 9], the overall conductance of the channel becomes quantized:

$$G = N \frac{2e^2}{h} \quad (3)$$

Here, N stands for the total number of the occupied transverse quantum confinement modes by the electrons in the channel, and spin degeneracy is assumed. This quantized conductance is fundamentally similar to the quantized Hall conductance at a high magnetic field: both are direct manifestations of one-dimensional electron transport [10]. Therefore, the quantum Hall effect has also been

elegantly described in the theoretical framework of the Büttiker–Landauer formalist [11].

It has been expected that devices based on ballistic electron transport have superb performance. Since electrons are free from random scattering events, ballistic electron devices may have a very high intrinsic working speed and a quick response. Secondly, the strongly temperature-dependent phonon scatterings, which in some cases lead to serious degradation in device performance in a traditional electron transport device, do not exist in a ballistic device by its nature. Therefore, ballistic devices in general are less temperature dependent.

It is easiest to realize ballistic electron transport at cryogenic temperatures using III–V compound semiconductor materials because of the long electron mean-free path obtained under both conditions. For example, l_e exceeding 160 μm has been observed in a high-quality GaAs–AlGaAs heterostructure at temperature $T = 0.1$ K [12]. Therefore, it is even possible to use conventional photolithography to fabricate devices smaller than l_e and realize ballistic transport at low temperatures. There have been a great number of studies on ballistic electron transport, and many striking phenomena were discovered in various types of ballistic devices. Examples are the above-mentioned quantized conductance in a point contact [8, 9], electron focusing experiments [13–16], negative bend resistance [17], quenched and negative Hall effects [18–20], and lateral hot ballistic electron devices [21, 22].

New transport properties realized in the ballistic transport regime have inspired inventions of novel device concepts. Many of the new concepts are based on the fact that the only scatterings that the ballistic electrons experience are those from the designed device boundaries. By simply tailoring the boundary of a ballistic device, the electron transport can be, to a large extent, modified and controlled. It is hence possible to generate new device functionalities by simply tailoring the device shape. In contrast, due to the nature of the diffusive electron transport, the properties of a traditional device are not sensitive to a change in the device boundary.

Despite great experimental efforts, only a small number of successful experiments have demonstrated ballistic transport at room temperature. From the application point of view, it is highly desirable that new types of ballistic devices are capable of operating at room temperature. At room temperature, the electron mean-free path in a III–V semiconductor heterostructure is typically from 100 to 200 nm. Device dimensions smaller than or at least comparable to l_e at $T = 300$ K are therefore required. This is, however, very difficult if using a GaAs–AlGaAs heterostructure due to the large depletion length (around 100 nm) close to the etched device boundary. The much shorter depletion length (below 30 nm) in, for example, InGaAs–InAlAs or InGaAs–InP material systems, makes it possible to fabricate much smaller devices that work at room temperature. In general, it is also easier to achieve a higher sheet carrier density in an InGaAs–InAlAs heterostructure (up to around $1 \times 10^{12} \text{ cm}^{-2}$) than in a GaAs–AlGaAs system. The higher carrier density not only reduces the depletion length, but also increases the Fermi velocity, and hence enhances the electron mean-free path.

Figure 3 schematically shows a device fabricated by Hirayama and Tarucha using an AlGaAs/InGaAs/GaAs

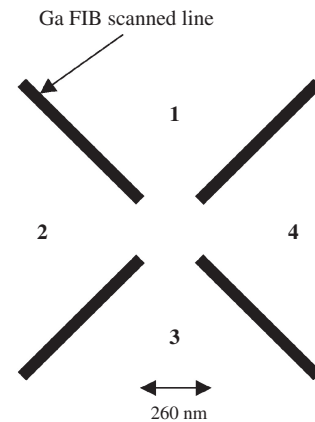


Figure 3. Schematic view of a device fabricated by Hirayama and Tarucha [23]. The four straight insulating lines (represented by the dark lines in the figure) were made by a focused Ga ion beam. Four electric contacts, numbered 1–4, were separated by the insulating lines.

modulation-doped heterostructure [23]. This is, to the author's knowledge, the first device that has been demonstrated to show ballistic electron transport properties at room temperature. The four straight insulated lines (represented by the dark lines in the figure) were made by a focused ion beam (FIB) of Ga. The FIB beam diameter was about 80 nm. The FIB scanned lines separated the four electric contacts, numbered 1, 2, 3, and 4.

During the experiments, Hirayama and Tarucha measured the so-called four-terminal bend resistance $R_{12,43} = V_{43}/I_{12}$ by sending a current I_{12} through contacts 1 and 2 and detecting the voltage between 4 and 3. If the electron transport is diffusive, the bend resistance $R_{12,43}$ would be positive. However, the experiment showed that $R_{12,43}$ was negative in the ballistic transport regime, which can be understood by considering the transmission coefficients of the ballistic electrons. Suppose that $I_{12} < 0$, and that electrons are ejected into the junction from contact 1. Instead of turning the corner between contacts 1 and 2 and transmitting into contact 2, the electrons enter the junction like billiard balls, and tend to go straight into contact 3. This results in an accumulation of electrons in contact 3, and therefore a positive V_{43} (instead of a negative voltage in a diffusive device) between contacts 4 and 3. The negative bend resistance is hence an indication of the existence of ballistic electron transport.

In the experiments, negative $R_{12,43}$ was observed from $T = 1.5$ K all the way up to room temperature, although the magnitude of the negative bend resistance was reduced by a factor of about 8 at $T = 290$ K. The result was interpreted in terms of the temperature-dependent mean-free path. At low temperature, l_e is much larger than the size of the junction in the center, and purely ballistic transport was realized. At $T = 290$ K, however, l_e is only about 135 nm, which is shorter than the length of the junction (260 nm), leading to the decrease of the magnitude of the negative bend resistance. Nevertheless, since the mean-free path at room temperature is still comparable to the length of the junction, some electrons still travel ballistically without being scattered when passing through the junction, although most electrons will experience at least one scattering event.

This is the reason why the bend resistance is still negative at room temperature. Furthermore, as Hirayama and Tarucha pointed out, at a higher temperature, more electrons will gain thermal energy above the Fermi level. These higher energy electrons might enhance the ballistic nature of the system. Recently, Hieke et al. similarly showed negative bend resistance in small cross junctions made from an InGaAs–InP modulation-doped quantum-well wafer [24]. The structures were fabricated by electron-beam lithography and deep dry etching. The experiments also indicated the partly ballistic electron transport in their devices at room temperature. Another important result of this study is the demonstration of low depletion length in such InP–InGaAs etched structures.

1.2. Nonlinear Ballistic Electron Transport

In this review, we focus on the recently demonstrated new types of ballistic devices that have been shown not only to operate at room temperature, but also to have great potentials in practical applications. All three types of devices are based on nonlinear ballistic electron transport, which is not at all simply by coincidence.

Nonlinear transport is particularly important in mesoscopic structures, and many striking phenomena discovered in ballistic devices are in the nonlinear regime, as shown in a number of experiments [25–40] and theoretical investigations [41–48]. First of all, a very small applied voltage suffices to drive the electron transport into the nonlinear regime. This is because of the small device dimension, and the fact that, in general, the applied voltage drops quite locally in the regions where the dimension of the electron path is changed, such as the opening and exit of a narrow channel, as mentioned earlier. Secondly, in a multiple-terminal ballistic device, the angular distribution of the electrons may largely determine the electron transmission probabilities between the terminals, and consequently, also the transport properties of the device. In contrast to the electron transport in a macroscopic semiconductor device, where the large number of scattering events completely randomize the direction of the electron velocities, a voltage applied to a ballistic device will change the angle of every electron in a predictable manner. As will be shown later, this has a direct influence on the transmission probabilities, and therefore also on the current distribution in the device. This is a new type of nonlinear effect which does not exist in a macroscopic device. In particular, it was recently realized that the geometrical symmetry of a ballistic device can also have a very pronounced influence on the nonlinear device properties [33–37]. One such example, which will be shown in Section 2, is called a ballistic rectifier. It is a completely new type of rectifying device because the nonlinear effect was based neither on a doping junction nor on a barrier structure. The ballistic rectifier has been demonstrated to operate at room temperature and at frequencies up to at least 50 GHz. A semiclassical model of the device is shown in Section 2.2.

Based on a similar working principle to the ballistic rectifier, a new class of nanostructured artificial material has also been constructed, as will be shown in Section 3. The nanomaterial turns out to be in analog with the so-called

photogalvanic crystals. It was discovered more than 30 years ago that some natural crystals can generate a direct electron current under uniform illumination [49–51]. Referred to as the photogalvanic effect, the phenomenon has been identified to be a macroscopic manifestation of the absence of centrosymmetry in the elementary crystal structure, despite the macroscopic homogeneity of these crystals. In this case, light serves as a source of external fluctuation by imposing an unbiased, time-periodic electric field on the crystals, and the generation of direct electron current can be viewed as an extremely fast rectification at the frequency of the light. Recently, similar geometries to those found in photogalvanic crystals were realized to be useful for biomolecular separation devices consisting of arrays of symmetry-breaking microscopic obstacles [52–55].

Furthermore, it is naturally expected that, if the device dimension is comparable to the electron wavelength, quantum effects will take place. For a narrow channel or a device with a narrow constriction such as a quantum point contact, an applied voltage changes both the phase of the electrons and the electron distribution among the transverse quantum confinement modes in the channel, hence leading to a change in the conductance. In Section 4, three-terminal ballistic devices based on such a nonlinear effect will be discussed. The effect can also be well described with an extended Büttiker–Landauer formula.

In Section 5, the recently discovered quantum behavior of nanometer-sized ballistic rectifiers at temperatures very close to room temperature will be presented. Quantum devices generally have the advantages of being ultrasensitive and ultrafast. The results indicated the promising possibility of realizing room-temperature operations of quantum-effect-based nanoelectronic devices.

After the review on these nonlinear, room-temperature ballistic devices, ranging from basic device physics and modeling to the device performance and prospects of real applications, we conclude with an outlook in Section 6 on expected future developments in this yet new, but promising field.

2. BALLISTIC RECTIFIERS AND SEMICLASSICAL MODEL

In this section, a new type of semiconductor rectifier is introduced. The device, referred to as a ballistic rectifier, is based on a completely different working principle from a semiconductor diode since no doping junction or barrier structure has been used. The rectifying effect relies on the nature of the ballistic electron transport, and also on tailoring the device geometry. After the experimental results shown in Section 2.1, a semiclassical model of nonlinear ballistic electron transport will be introduced in Section 2.2, which yields an analytical description of the ballistic rectifying effect.

2.1. Experimental Results

There were quite a number of studies on mesoscopic semiconductor cross junctions in the early days of the realization of ballistic transport. A variety of novel phenomena have been observed in such devices, such as electron focusing

[13–15], negative bend resistances [17], and the quenched or negative Hall effect [18, 19]. While these experiments were performed in the linear transport regime, a ballistic rectifier operates in the nonlinear regime. Furthermore, a triangular scatterer was introduced to break the device symmetry which, as shown below, plays a key role in generating the rectifying effect. Figure 4(a) is an atomic force microscope image of the central part of one of the first ballistic rectifiers [34]. The dark areas in Figure 4(a) are the regions that were etched away and became insulating for the electrons. As a result, the triangular antidot was defined in the cross junction, which consists of the two narrow channels (labeled “source” S and “drain” D) and the two wide channels (labeled “upper” U and “lower” L). The triangular antidot acted as an artificial scatterer which, as shown in the following, induced a pronounced nonlinear effect.

The modulation-doped GaAs-AlGaAs heterostructure, from which the ballistic rectifier was fabricated, contains a two-dimensional electron gas (2DEG) located 37 nm below the wafer surface. The sheet density of the 2DEG is about $5 \times 10^{11} \text{ cm}^{-2}$ and the mobility is about $5 \times 10^5 \text{ cm}^2/\text{V} \cdot \text{s}$ at a temperature $T = 4.2 \text{ K}$. Standard electron-beam lithography and wet chemical etching are used in the fabrication. Since the electron mean-free path $l_e = 5.8 \mu\text{m}$ is longer than the central part of the device, the electron transport is ballistic at 4.2 K.

Like a typical four-terminal measurement, the (input) current is applied through leads S and D , and the output voltage is detected via L and U . The typical electron trajectories, illustrated by the arrows in Figure 4(a), suggest an accumulation of electrons in the lower lead, and hence a negative voltage between L and U . Obviously, this cannot happen when the applied voltage or current is zero since the same number of electrons will go along the opposite directions of the arrows. For a nonzero applied current, $I_{SD} \neq 0$; however, as shown by a detailed model [47, 56], the electron transmission along the arrows in Figure 4(a) is changed by the applied electric field, while the transmission in the reversed direction is virtually unaffected (details in Section 2.2). This gives rise to a finite negative voltage between L and U , V_{LU} .

Even though the mirror symmetry along the S - D axis is broken by the triangular antidot, the symmetry along the central L - U axis remains. As a consequence, the output voltage V_{LU} is expected to remain the same if the sign of

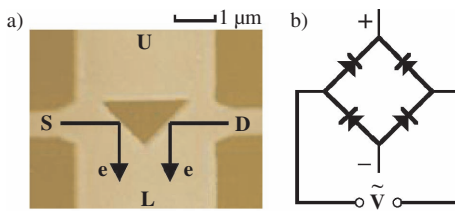


Figure 4. (a) Atomic force microscope image of the central part of a ballistic rectifier. The dark areas were etched away, forming the triangular antidot in the middle and the four channels S , D , L , and U . The current is applied via S and D , and the output voltage is measured between L and U . The device operates similarly to a bridge rectifier (b), but the ballistic rectifier is based on a completely new working principle. Adapted from [34].

the applied current I_{SD} is changed, that is,

$$V_{LU}(I_{SD}) = +V_{LU}(-I_{SD}). \quad (4)$$

Correspondingly, $R_{SD,LU}(I_{SD}) = -R_{SD,LU}(-I_{SD})$, where $R_{SD,LU} = V_{LU}/I_{SD}$ is the four-terminal resistance. Such a picture is almost perfectly supported by the experimental V_{LU} versus I_{SD} curves at $T = 4.2 \text{ K}$ (solid line) and 77 K (dotted line) shown in Figure 5. The slight deviation from Eq. (4) is attributed to the unintentional breaking of the desired symmetry along the L - U axis by the imperfection of the fabrication. The imperfection is expected to contribute mainly a linear term to the V_{LU} versus I_{SD} curves, in a way similar to a change of one of the four resistors in an otherwise balanced resistor bridge.

The experimental results demonstrate that new device functionalities can be realized by simply tailoring the shape of a ballistic device because the only scattering events that the electrons undergo are from the device boundary. The device shown in Figure 4, called a ballistic rectifier, operated similarly to a bridge rectifier [see Fig. 4(b)], but the working principle is completely different. First, only a single device is used here rather than four diodes in the bridge rectifier. The mechanism is also entirely different since no doping junction or barrier structure along the current direction is used in the ballistic rectifier. The pronounced nonlinear effect comes from the breaking symmetry and the properties of the ballistic electron transport. Furthermore, as will be shown in Section 2.2, the ballistic rectifier has no intrinsic voltage or current threshold, and can be used for the detection of very weak signals without the need of an external bias.

The nonlinearity in the I - V characteristics is remarkably different from that of a two-terminal nonlinear device, such as a diode, where the nonlinearity always appears on top of a large linear term. For the ballistic rectifier with the four-terminal geometry, there can be, however, no linear term present in the relationship between the output voltage and the applied current, as shown by Eq. (4). The striking nonlinearity is a result of the broken symmetry along the S - D axis and the mirror symmetry along the U - L axis.

As the temperature was increased from 4.2 K, the electron scattering from phonons increased, resulting in a lower

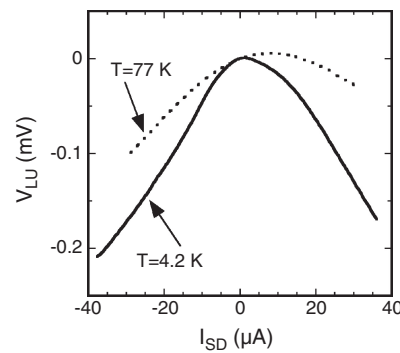


Figure 5. The output voltage between the lower and upper leads V_{LU} as a function of the input current through the source and drain leads I_{SD} measured at $T = 4.2 \text{ K}$ (solid line) and 77 K (dotted line). Ideally, the curves should be perfectly symmetric with respect to the vertical axis at $I_{SD} = 0$. However, the imperfection in the fabrication caused the slight asymmetry in the curves. Adapted from [34].

electron mobility and a shorter mean-free path. At $T = 77$ K, a weaker rectification than that at 4.2 K was observed, as shown by the dotted line in Figure 1(a). The less pronounced nonlinear behavior was attributed to the shorter l_e (about 1–2 μm) at 77 K. Since l_e was comparable to the distance between the openings of the S or D channels and the antidot, the electron transport was only partially ballistic.

To function at room temperature, a device size smaller than l_e (about 100 nm) at $T = 300$ K is required. It is very difficult to use wet chemical or dry etching to fabricate such small devices using a GaAs-AlGaAs heterostructure, due to the large depletion length close to etched device boundaries. The much shorter depletion length of the InGaAs-InP material system makes it possible to fabricate much smaller devices that work at room temperature [57]. The wafer that was used to fabricate the room-temperature ballistic rectifiers was a modulation-doped $\text{In}_{0.75}\text{Ga}_{0.25}\text{As}$ –InP quantum-well structure [58] grown by a metalorganic vapor-phase epitaxy at a pressure of 50 mbar and a temperature of 600 °C. Si was used as the dopant because of its slow carryover effect. The structure consists of a semi-insulating (001) InP substrate, a 250 nm, not intentionally doped buffer layer, a 9 nm thick $\text{In}_{0.75}\text{Ga}_{0.25}\text{As}$ quantum well, a 10 nm thick, undoped InP spacer layer, and a 35 nm thick InP layer doped by Si to a level of about $6 \times 10^{17} \text{ m}^{-3}$. On top of the doped layer, an additional 10 nm thick, undoped InP layer was grown. At room temperature, the carrier density of the two-dimensional electron gas in the $\text{In}_{0.75}\text{Ga}_{0.25}\text{As}$ quantum well is $4.7 \times 10^{15} \text{ m}^{-2}$ and the mobility $1.2 \text{ m}^2/\text{V} \cdot \text{s}$, corresponding to $l_e = 140$ nm. Figure 6 shows the scanning electron microscope images of two room-temperature ballistic rectifiers with different sizes. Since l_e is only slightly shorter than the distance from the S or D channel to the triangular antidot, a large number of electrons can still travel through this distance without being scattered. As shown by Hirayama and Tarucha [23], if the electron transport is partially ballistic, the ballistic effect may still be observed, although weaker than that at low temperatures. Here, instead of a dc current, an ac voltage (1 kHz) was applied to the device, the dc (or average) voltage between the lower and upper terminals was measured. Indeed, a rectification efficiency of about 14% at room temperature, roughly half of that at 100 K, was observed in the smallest ballistic rectifier, as shown in Figure 7. This is one of the very few types of novel

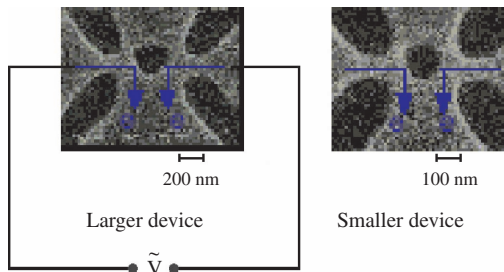


Figure 6. Scanning electron microscope images of two room-temperature ballistic rectifiers with different sizes, fabricated from an InGaAs-InP heterostructure. Reprinted with permission from [57], A. M. Song et al., *Jpn. J. Appl. Phys.* 40, L909 (2001). © 2001, Japan Society of Applied Physics.

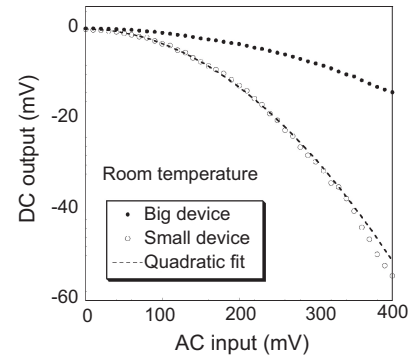


Figure 7. Room-temperature operation of the ballistic rectifiers shown in Figure 6. The frequency of the input ac signal is 1 kHz. The dashed line represents a quadratic fit to the experimental result of the smaller rectifier. Reprinted with permission from [57], A. M. Song et al., *Jpn. J. Appl. Phys.* 40, L909 (2001). © 2001, Japan Society of Applied Physics.

nanodevices that have so far been shown to work at room temperature.

Apart from meeting the criterion of functioning at room temperature, for possible real applications, any new type of nanodevice is desirable to function at gigahertz frequencies. To investigate the speed of the ballistic rectifiers, high-frequency experiments up to 50 GHz have been performed. Because of the in-plane nature of the ballistic rectifier—the electrical contacts are laterally separated rather than placed on the surface and the back side (substrate)—the parasitic capacitance between contacts is substantially lower than in a conventional vertical device of the same size. Furthermore, the new working mechanism does not rely on any minority carrier diffusion or barrier structure, two factors that often limit the speed of conventional semiconductor diodes. The ballistic rectifier was therefore expected to function at very high frequencies. Figure 8 shows the dc output of the device versus the power of 50 GHz signal at room temperature. The 50 GHz signal was transmitted to the device via a coplanar probe. The power (horizontal axis) in Figure 8 was the output power from the signal source. Due to the impedance

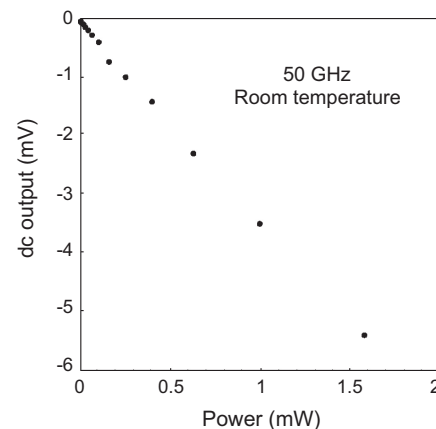


Figure 8. Output dc voltage of the smaller ballistic rectifier shown in Figure 6(b) versus the power of the applied 50 GHz signal at room temperature. Reprinted with permission from [57], A. M. Song et al., *Jpn. J. Appl. Phys.* 40, L909 (2001). © 2001, Japan Society of Applied Physics.

mismatch between the signal source ($50\ \Omega$) and the device (a few kilohms), as well as some power loss due to the cables at 50 GHz, effectively only a small fraction of the power from the signal source was actually applied to the device. It was estimated that the real sensitivity of the device at 50 GHz was a few hundred millivolts of dc output per milliwatt input, which is virtually as high as that of a commercial microwave detection diode [57]. The ballistic rectifiers were, however, not specifically optimized. Much improvement can be expected in the future, by, for example, further reducing the device size. For a device about half of the one shown in Figure 7, one can expect not only a much higher efficiency, but also a stable performance that is insensitive to temperature changes up to room temperature.

As will be shown in the next section, theoretical studies on the ballistic rectifier yielded a quadratic response to input signals, which is very different from the exponential current–voltage characteristic of a conventional semiconductor diode. In Figure 7, a fit of $y = ax^2$ (where y represents the dc output voltage, x the ac input voltage, and a a constant) was performed. The remarkably good fit supports the theoretical prediction of the quadratic response to input voltage, Eq. (18), which will be derived in Section 2.2. This unique characteristic allows for generating second-harmonic signals without producing third or higher harmonics. The polarization of the generated second-harmonic signal (along the vertical direction) is perpendicular to that of the input signal (horizontal direction), which makes the separation of the second harmonic from the input signal much easier. Because of the quadratic characteristic, one also expects that the dc output is a linear function of the applied microwave power, which is demonstrated in Figure 8. Although we have not been able to test the devices at frequencies higher than 50 GHz so far, it is expected, from the working principle, that the cutoff frequency will be much higher, possibly up to hundreds of gigahertz or even in the terahertz regime. Recent numerical simulations confirmed this expectation, and showed excellent performance of the ballistic rectifier as a frequency doubler or power detector in the terahertz regime [59].

2.2. Semiclassical Model

As discussed in Section 1, Ohm's law does not hold in ballistic devices. Instead, the Büttiker–Landauer formalism [5–7], which treats transport in mesoscopic conductors as a transmission problem for carriers at the Fermi level, is widely used to describe the linear transport behavior of these conductors [13–15, 17–20]. For a multiterminal ballistic conductor at $T = 0$, the current in lead α in the linear transport regime can be written as

$$I_\alpha = \frac{2e}{h} \sum_{\beta \neq \alpha} T_{\beta \leftarrow \alpha} (\mu_\alpha - \mu_\beta) \quad (5)$$

Here, I_α is the current through lead α , and μ_α is the chemical potential of the electrons in contact (carrier reservoir) α . Such a standard formula is for linear electron transport only because the transmission coefficient $T_{\beta \leftarrow \alpha}$ for electrons from terminal (contact) α to terminal β is not considered a function of the applied voltage. To model the nonlinear (rectifying) effect observed in the ballistic rectifiers and the artificial

nonlinear materials to be discussed in Section 3, the standard Büttiker–Landauer formula has been extended to the nonlinear regime. By doing so, a detailed model has been obtained, which provides analytical descriptions of the ballistic rectification effect in the framework of semiclassical ballistic electron transport [47].

Consider a general case where the electron transport is in the nonlinear regime, at a finite temperature, and in a finite magnetic field. The current through a lead α of a mesoscopic conductor, which is connected via perfect leads to a number of carrier reservoirs, can be written as

$$I_\alpha = \frac{2e}{h} \sum_{\beta \neq \alpha} \int [f(E - \mu_\alpha) - f(E - \mu_\beta)] \times T_{\beta \leftarrow \alpha}(E, B) dE \quad (6)$$

Here, $f(E - \mu_\alpha) = [\exp((E - \mu_\alpha)/k_B T) + 1]^{-1}$ is the Fermi–Dirac distribution function, and in general, the transmission coefficient for carriers from lead α to lead β , $T_{\beta \leftarrow \alpha}(E, B)$, is a function of the electron energy E and magnetic field B . At $k_B T = 0$ and $B = 0$, Eq. (6) becomes

$$I_\alpha = \frac{2e}{h} \sum_{\beta \neq \alpha} \bar{T}_{[\beta, \alpha]} (\mu_\alpha - \mu_\beta) \quad (7)$$

Here, $\bar{T}_{[\beta, \alpha]}$ equals $\int_{\mu_\beta}^{\mu_\alpha} T_{\beta \leftarrow \alpha}(E) dE / (\mu_\alpha - \mu_\beta)$ if $\mu_\alpha > \mu_\beta$, and $\int_{\mu_\alpha}^{\mu_\beta} T_{\alpha \leftarrow \beta}(E) dE / (\mu_\beta - \mu_\alpha)$ otherwise. This shows that only the transmissions from the reservoirs with higher chemical potentials to the reservoirs with lower chemical potentials need to be considered. Based on Eq. (7), the ballistic rectifying effect can be modeled in the framework of semiclassical ballistic electron transport.

Similar to the model for ballistic electron transport in a cross junction by Beenakker and van Houten [60], only the angular distribution of the ballistic electrons ejected from S and D was taken into account to determine the electron transmission probabilities into L or U leads. This is a particularly good approximation for this specific device geometry because the transmission probabilities for electrons from S (or D) to L and U are virtually completely determined by the ejection angles of the electrons.

First, consider the device at equilibrium, that is, when no voltage is applied. The angular distribution of the electrons ejected from a narrow constriction, for example, of the S and D channels, is given by

$$P(\theta) = \frac{1}{2} \cos \theta \quad (8)$$

Here, θ is the ejection angle with respect to the channel direction. Therefore, even at $V_{SD} = 0$, the electrons ejected out of S are, to some extent, collimated, as shown in Figure 9(c). This is actually a property of ballistic electrons, caused by the adiabatic electron transport at sufficiently low temperatures and in channels with smooth boundaries at the entrances and exits [14, 20, 61, 62].

Let θ_0 be the minimum ejection angle for an electron from S or D to be scattered by the triangular antidot to the lower lead. For the specific device in Figure 4, which is to

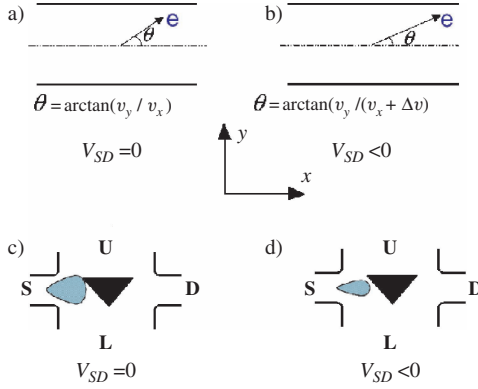


Figure 9. (a) The sketch shows that, at $I_{SD} = 0$, an electron is moving in the source channel with the angle $\arctan(v_y/v_x)$, where v_x and v_y are the velocity components along the direction of the channel and in the perpendicular direction. (b) When a negative voltage V_{SD} is applied, $I_{SD} < 0$, corresponding to a finite drift velocity Δv of the electrons in the source channel. This leads to a smaller ejection angle of the electron $\arctan[v_y/(v_x + \Delta v)]$. Overall, this results in a collimation effect induced by the applied voltage, and the angular distribution of the electron ejected out of S at $V_{SD} = 0$ shown in (c) becomes narrower at $V_{SD} < 0$, as schematically shown in (d). Consequently, the electrons more likely will be scattered by the triangular antidot to the lower lead, and have less chance to go through the gap between the antidot and the edge of the upper channel. This results in an accumulation of electrons in the lower lead, and consequently a negative voltage V_{LU} .

be modeled below as an example, $\theta_0 \approx \pi/4$. From Eq. (8), it is easy to obtain the transmission coefficients at zero bias:

$$T_{L \leftarrow S} = T_{L \leftarrow D} = T_{D \leftarrow L} = T_{S \leftarrow L} = N_{SD} \int_{-\pi/2}^{\theta_0} P(\theta) d\theta = \frac{N_{SD}(1 + \sin \theta_0)}{2} \quad (9a)$$

$$T_{U \leftarrow S} = T_{U \leftarrow D} = T_{D \leftarrow U} = T_{S \leftarrow U} = N_{SD} \int_{\theta_0}^{\pi/2} P(\theta) d\theta = \frac{N_{SD}(1 - \sin \theta_0)}{2} \quad (9b)$$

Here, N_{SD} is the number of occupied transverse quantum confinement modes at the Fermi level E_F in channels S and D .

To obtain an analytical description of the ballistic rectifying effect, certain approximations have to be taken. Ideally, the potential profile in the device at a finite I_{SD} should be calculated self-consistently in order to obtain the angular distribution of the ballistic electrons, and hence the transmission coefficients. Such a calculation is, however, very complex. Instead, it is noticed that the applied voltage mainly drops at the entrances and exists of the S and D channels [4]. Consider that, at $V_{SD} = 0$, the velocity components of a right-moving electron in the source channel are v_x and v_y , respectively, in the direction of the channel and in the perpendicular direction, as illustrated in Figure 9(a). The angle of ejection $\theta(I_{SD} = 0) = \arctan[v_y/v_x]$ will change if a finite V_{SD} is applied. For example, if V_{SD} is negative, the current in the source channel $I_S < 0$, meaning that the electrons in the source channel have a finite mean velocity or drift velocity, $\Delta v > 0$. As a good approximation, assume that the velocity component in the x direction of

all of the electrons in channel S is increased by Δv , while the velocity component in the perpendicular direction v_y is essentially not affected. The ejection angle of the electron changes from $\arctan[v_y/v_x]$ at $I_{SD} = 0$ to a smaller angle $\arctan[v_y/(v_x + \Delta v)]$, as shown in Figure 9(b). Overall, this leads to a collimation effect induced by the applied voltage, which effectively narrows the angular distribution of the electron ejected out of S at $V_{SD} < 0$, as schematically shown in Figure 9(d).

The changes of the transmission coefficients, which fundamentally determine the output V_{LU} , can be directly evaluated once the angular distribution of the electrons is known. Since the angular distribution of the electrons ejected out of S becomes narrower, the electrons will have a greater chance to be scattered into the lower lead by the triangular antidot, and therefore the transmission probability for the ejected electrons to transmit from S to L will increase. In the meantime, the transmission probability from S to U will decrease since the probability for the electrons to have a large enough ejection angle to transmit through the gap between the antidot and the edge of the upper channel will reduce. The above analysis shows that the transmission probabilities of electrons could be directly linked to the electron drift velocity, and hence I_{SD} . It can be shown that

$$T_{L \leftarrow S}(I_{SD} < 0) - T_{L \leftarrow S}(I_{SD} = 0) = \frac{N_{SD}}{2} (\sin \theta_e - \sin \theta_0) \quad (10a)$$

$$T_{U \leftarrow S}(I_{SD} < 0) - T_{U \leftarrow S}(I_{SD} = 0) = -\frac{N_{SD}}{2} (\sin \theta_e - \sin \theta_0) \quad (10b)$$

In the equations, θ_e is determined by

$$\theta_e = \theta_0 + \arcsin[(\Delta v/v_F) \sin \theta_0] \quad (11)$$

where v_F is the Fermi velocity [47]. Assuming a hard wall potential for the source and drain channels because of the relatively large channel width, it can be shown that

$$\frac{\Delta v}{v_F} = -\frac{\hbar}{N_{SD} e E_F} I_{SD} \quad (12)$$

Here, the changes in the number of occupied modes in the source and drain channels with applied bias are neglected. This is, however, a good approximation for the four-terminal measurements of the ballistic rectifier. As will be shown by the following analysis, the output of a ballistic rectifier is determined by the relative changes of the transmission coefficients $\Delta T/T$ rather than the absolute values of the changes in the transmission coefficients ΔT .

Shown in Figure 10 is the dependence of the transmission coefficients on the electric current of the lead from which the electrons are ejected. Therefore, Eq. (7) can then be written as

$$I_\alpha \approx \frac{2e}{h} \sum_{\beta \neq \alpha} \bar{T}_{[\beta, \alpha]}(I_{[\beta, \alpha]})(\mu_\alpha - \mu_\beta) \quad (13)$$

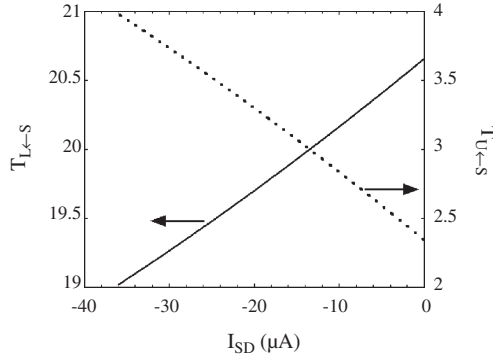


Figure 10. Calculated transmission coefficients $T_{L \leftarrow S}$ and $T_{U \leftarrow S}$ as a function of the negative source-drain current at $T = 0$. Adapted from [47].

where $\bar{T}_{[\beta, \alpha]}(I_{\{\beta, \alpha\}})$ equals $\bar{T}_{\beta \leftarrow \alpha}(I_\alpha)$ if $\mu_\alpha > \mu_\beta$ and $\bar{T}_{\alpha \leftarrow \beta}(I_\beta)$ otherwise [47]. With the values of the transmission coefficients determined, the V_{LU} versus I_{SD} characteristic is obtained by calculating the four-terminal resistance $R_{SD, LU} = V_{LU}/I_{SD}$. For the case of $V_{SD} < 0$,

$$\begin{aligned} R_{SD, LU} &= \frac{\hbar[T_{L \leftarrow S}(I_S)T_{D \leftarrow U}(I_U) - T_{D \leftarrow L}(I_L)T_{U \leftarrow S}(I_S)]}{2e^2 D} \\ &= \frac{\hbar[T_{L \leftarrow S}(I_{SD})T_{D \leftarrow U}(0) - T_{D \leftarrow L}(0)T_{U \leftarrow S}(I_{SD})]}{2e^2 D} \end{aligned} \quad (14)$$

where $I_S = I_{SD}$ and $I_L = I_U = 0$. Therefore, because the net current in L and U is zero, $T_{D \leftarrow L}$ and $T_{D \leftarrow U}$ are not sensitive to the applied current I_{SD} , and their values at zero bias are employed. In Eq. (14), D is a function of the individual transmission coefficients, and is found to be insensitive to the applied voltage or current [63]. For this specific device, $\theta_0 \approx \pi/4$, $T_{S \leftarrow D} = T_{D \leftarrow S} = 0$, and $T_{L \leftarrow U} \approx N_{LU}/3$, where N_{LU} is the number of occupied transverse quantum confinement modes in channels L and U . With these relations and taking into account $N_{LU} \gg N_{SD}$, it can be shown that

$$\begin{aligned} D &= N_{SD}[2T_{L \leftarrow S}T_{U \leftarrow S} + T_{L \leftarrow U}N_{SD}] \\ &\approx \frac{N_{SD}^2 N_{LU}}{3} \end{aligned} \quad (15)$$

Substituting Eqs. (9), (10), and (15) into Eq. (14) yields

$$V_{LU} = R_{SD, LU}I_{SD} = \frac{3h}{4e^2} \frac{\sin \theta_e - \sin \theta_0}{N_{LU}} I_{SD} < 0 \quad (16)$$

Note that θ_e is a function of I_{SD} , as shown by Eqs. (11) and (12). Combining the above with the case of $V_{SD} > 0$, where V_{LU} is also found to be negative, we have

$$V_{LU} = -\frac{3h}{4e^2} \frac{\sin \theta_e - \sin \theta_0}{N_{LU}} |I_{SD}| \quad (17)$$

The V_{LU} versus I_{SD} curve, calculated analytically for the device shown in Figure 4(a), is plotted with the solid line in Figure 11. It is in very good agreement with the experimental result (dashed line), especially in the low-current region. No adjustable parameters have been used at all in Eq. (17). At high currents, electron heating, not included in the above model, might reduce the rectifying effect. Moreover, the

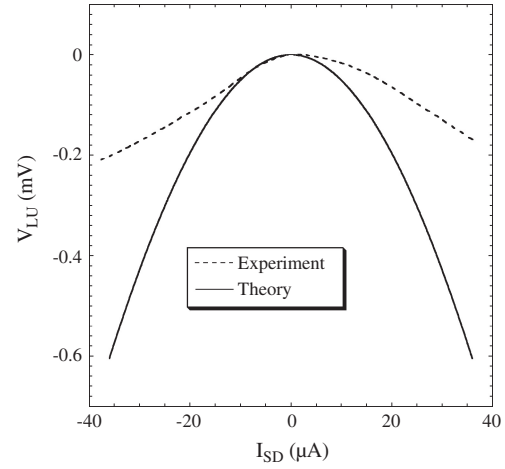


Figure 11. Theoretical (solid line) and experimental (dashed line, the same as that in Fig. 5) V_{LU} versus I_{SD} curves for the device shown in Figure 4(a). Although no fitting parameters have been used, the agreement between the experiment and the model is remarkably good. Reprinted with permission from [71], A. M. Song, *Appl. Phys. A* 75, 229 (2002). © 2002, Springer-Verlag.

length of the L and U channels ($5 \mu\text{m}$) is comparable to the electron mean-free path. This means that some electrons will be scattered by impurities or phonons, and change directions before they can travel through the channels and enter the electrical contact regions (carrier reservoirs). This certainly causes a reduced output.

The curves in Figure 10 display the dependence of $T_{L \leftarrow S}$ and $T_{U \leftarrow S}$ on I_{SD} . From $I_{SD} = 0$ to $-37 \mu\text{A}$, $T_{L \leftarrow S}$ increases by about 6.4%, while $T_{U \leftarrow S}$ decreases by about 34%. From Eq. (14), it is clear that, although the magnitude of the transmission from S to U is much less than that from S to L , it has a much stronger influence on $R_{SD, LU}$, and therefore contributes much more to the observed negative output V_{LU} .

It is also interesting to note that, in the limit as $|I_{SD}| \rightarrow 0$, V_{LU} can be shown to have a quadratic response to I_{SD} [47]:

$$V_{LU} = -\frac{3\pi\hbar^2}{4e^3 E_F N_{SD} N_{LU}} I_{SD}^2 \quad (18)$$

Although the modeling was performed under the condition of $T = 0$, it has been shown that Eq. (18) holds as well at a finite temperature for sufficiently small currents [64], meaning that there is no threshold or turn-on voltage for the ballistic rectifier. With respect to applications, it is interesting to note that there are a number of practical advantages associated with the quadratic response, as have been introduced in Section 2.1 and will be discussed in Section 3. Based on the above picture, the nonlinear ballistic electron transport at finite magnetic fields can also be well described [65].

3. ARTIFICIAL FUNCTIONAL NANOMATERIALS

The concept of the ballistic rectifier has been extended from a single device to a new type of artificial functional material [66]. Figure 12 shows the atomic force microscope images of two examples of the artificial material that have been made.

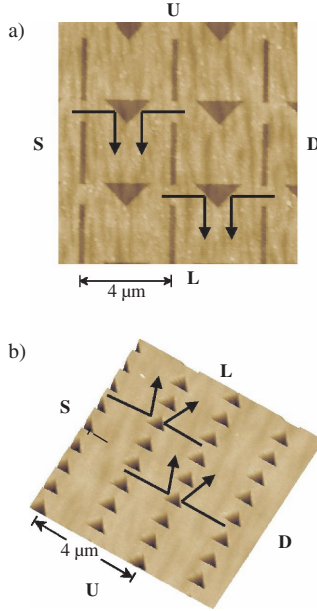


Figure 12. Atomic force microscope images of artificial functional materials of two different designs, fabricated using a GaAs-AlGaAs heterostructure. Note that the L terminal is on the upper-right side in (b). The arrows indicate the typical electron trajectories in the artificial materials.

The working principle of the nonlinear materials is similar to that of the ballistic rectifier, and the materials were also fabricated using standard electron-beam lithography and wet chemical etching. In Figure 12(a), the artificial material was constructed by simply duplicating a ballistic rectifier over space. The duplicated individual rectifiers were connected in series and parallel, forming a network or an “artificial lattice.” Apart from the above design, a material shown in Figure 12(b) was also fabricated, which only consisted of triangular antidots. In the material, not only is the intentionally broken symmetry by the triangular antidots important, but also the introduced offset between neighboring columns: the triangles were placed in such a coherent way that neighboring triangles support each other by simultaneously scattering electrons and forming channels through which electrons were ejected, as shown by the arrows in Figure 12(b).

In principle, these artificial materials can be made over a whole wafer. One apparent advantage is that the material is suitable for applications involving large signals, as a much higher voltage or current can be applied. Compared with the fabrication of a diode which involves multiple-step mask alignment, the production of the nanomaterial involves only one step of lithography. Therefore, the recently invented nanoimprint technology [67] can be used to mass produce these materials. It allows us to avoid the bottleneck of extremely long e-beam exposure time, a challenging problem in producing a large number of nanodevices efficiently and economically. With the nanoimprint technology, a master stamp (mold) with e-beam lithography can be used to replicate patterns over whole wafers of up to 6 in. in a matter of minutes [68]. Furthermore, for radio-frequency (gigahertz or even terahertz) applications, such as RF detection (the capability of the material to function at up to at

least 50 GHz will be discussed later), it is often desirable to have a detector with a large active region in order to eliminate the need for building antennas. Moreover, as the nanomaterial is intrinsically nonlinear, individual devices can be made by simply cutting pieces from the material, according to the requirements for different applications.

The measurements on the artificial materials are very similar to those on the ballistic rectifier. An $80 \times 80 \mu\text{m}^2$ piece of the artificial material shown in Figure 12(b) has been measured at $T = 4.2 \text{ K}$. To study how the nonlinear effect changes with the electron concentration or the electron Fermi wavelength, a layer of metal gate was evaporated on top of the artificial material after etching the triangular antidots. Negative gate voltages V_{GU} were applied between the gate and U to lower the carrier concentration of the 2DEG and increase the Fermi wavelength of the electrons. The lowered carrier concentration was directly indicated by the increase of the two-terminal source-drain resistance R_{SD} , as shown in Figure 13(c). From the figure, the pinch-off gate voltage is about -2.25 V . Figure 13(a) shows the V_{LU} versus I_{SD} curves measured at different gate voltages V_{GU} at $T = 4.2 \text{ K}$. Similar to the experimental results of the ballistic rectifiers in Figure 5, the curves are not perfectly symmetric with respect to the vertical axis at $I_{SD} = 0$, which is a consequence of the imperfect device fabrication. The overall downward bending of the curves clearly indicates the expected rectifying effect. To better illustrate the influence of the gate voltage on the rectifying effect, the average output V_{LU} at $I_{SD} = +37 \mu\text{A}$ and $I_{SD} = -37 \mu\text{A}$ is plotted as a function of the applied gate voltage V_{GU} in Figure 13(b). The curve shows that the rectifying effect was enhanced dramatically by increasing the applied negative gate voltage. In particular, the average output increased rapidly when

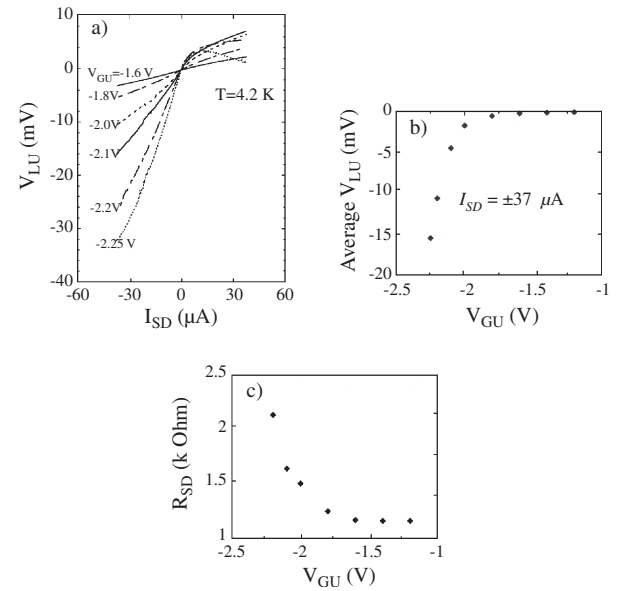


Figure 13. (a) V_{LU} versus I_{SD} curves at different voltages between the gate G and terminal U , V_{GU} , measured in an $80 \times 80 \mu\text{m}^2$ piece of the artificial material shown in Figure 12(b) at $T = 4.2 \text{ K}$. (b) The average output voltage V_{LU} at $I_{SD} = +37 \mu\text{A}$ and $I_{SD} = -37 \mu\text{A}$ as a function of V_{GU} . (c) The two-terminal source-drain resistance R_{SD} as a function of V_{GU} .

V_{GU} was approaching the pinch-off gate voltage of about -2.25 V.

The rectifying effect observed in the artificial material shown in Figure 13 can be qualitatively explained in the same physical picture. Similar to the voltage-induced collimation effect shown in Figure 9, the angular distribution of the electrons ejected out of the narrow gaps between neighboring triangular antidots at $V_{SD} = 0$ illustrated in Figure 14(a) becomes narrower at $V_{SD} < 0$, as schematically shown in Figure 14(b). The angular distribution is tilted upwards a little because of the asymmetry of the geometry [62, 69]. This leads to a higher probability for the electrons to be deflected downwards by the next triangular antidot on the side, as schematically shown in Figure 14(b), and fewer electrons will be able to transmit upwards. This induces an accumulation of electrons at the lower contact, and therefore a negative output voltage V_{LU} .

The pronounced gate-voltage dependence shown in Figure 13(a) and (b) is expected from the above model for the ballistic rectifier, although strictly speaking, Eq. (18) does not hold for the artificial material. However, since the working principle is the same, it could be used to qualitatively analyze the experimental results of the artificial material. For the material shown in Figure 12(b), by decreasing the voltage on the top gate, the electron density, and therefore E_F , reduces. From Eq. (18), the output voltage $|V_{LU}|$ will increase. Moreover, the lowered E_F also means less electron occupation of the transverse confinement modes in the gaps between neighboring triangular antidots. This can be regarded as reducing N_{SD} in Eq. (18), which also contributes to the dramatic increase of $|V_{LU}|$ in Figure 13.

Both of the artificial materials shown in Figure 12(a) and (b) could work only at temperatures below 77 K because of the large “lattice constants.” It is possible to achieve room-temperature operations of the artificial material by fabricating nanomaterials with artificial lattice constants comparable to, or shorter than, the electron mean-free path [70]. Figure 15(a) is an atomic force microscope image of one of the nanomaterials that operates at room temperature, fabricated from the same InGaAs-InP heterostructure that was used to fabricate the room-temperature ballistic rectifiers. The lattice constants of the nanomaterial are $a_x = 800$ nm and $a_y = 300$ nm in the lateral and vertical directions, respectively. Both the base and the height of the triangular antidots are 150 nm. The experimental data at room temperature are shown in Figure 15(b), in which the dc output between contacts L and U was measured as a function

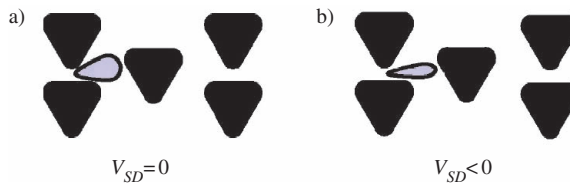


Figure 14. Similarly to the voltage-induced collimation effect shown in Figure 9, the angular distribution of the electrons ejected out of the narrow gaps between neighboring triangular antidots at $V_{SD} = 0$ (a) becomes narrower at $V_{SD} < 0$, as schematically shown in (b). The angular distribution is tilted upwards a little because of the asymmetry of the geometry.

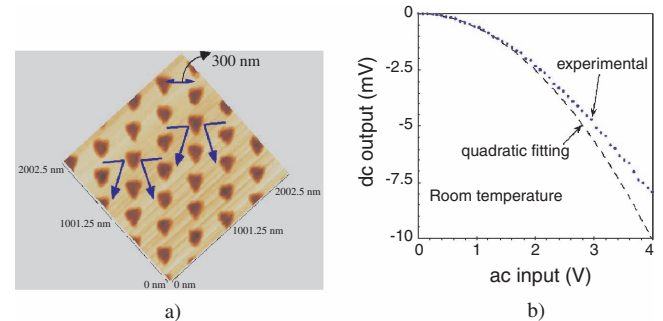


Figure 15. (a) Atomic force microscope image of one of the nanomaterials that operates at room temperature. The arrows represent typical electron trajectories. The lattice constants of the “artificial lattice” are $a_x = 800$ nm and $a_y = 300$ nm in the lateral and vertical directions, respectively. Both the base and the height of the triangular antidots are 150 nm. (b) Experimental data of a $30 \mu\text{m} \times 30 \mu\text{m}$ piece of the nanomaterial shown in (a) at room temperature, in which the dc output between the lower and upper contacts was measured as a function of the applied low-frequency (1 kHz) ac signal. The dashed line represents a quadratic fit. Reprinted with permission from [71], A. M. Song, *Appl. Phys. A* 75, 229 (2002). © 2002, Springer-Verlag.

of the applied low-frequency (1 kHz) ac signal. The experiment was performed using a $30 \mu\text{m} \times 30 \mu\text{m}$ piece of the nanomaterial [71]. Note that the feature size of the nanomaterial is still far from ideal, that is, both a_x and a_y would ideally be shorter than l_e . The room-temperature operation shown in Figure 15(b) may be greatly improved by fabricating nanomaterials with a smaller feature size using the state-of-the-art nanolithography.

Similar to a ballistic rectifier, the in-plane nature of the nanomaterial ensures that the parasitic capacitance between contacts is much lower than in a conventional vertical device of the same size. The nanomaterial thus has an extremely high working speed, as is evident in high-frequency experiments. The curve in Figure 16 shows the output dc voltage between the contacts L and U as a function of the RF power of a 50 GHz signal, which was transmitted to the

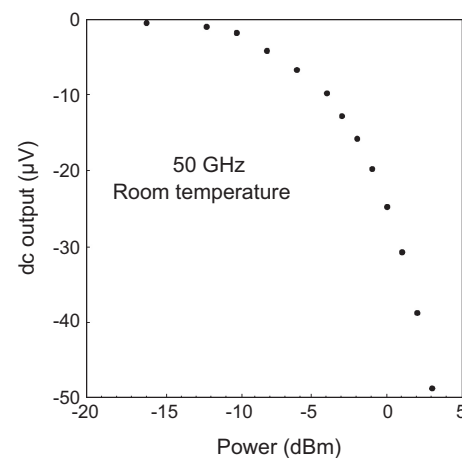


Figure 16. Output dc voltage of the nanomaterial versus the power of the applied 50 GHz signal at room temperature. The RF signal was applied to the material via coplanar probes. Reprinted with permission from [71], A. M. Song, *Appl. Phys. A* 75, 229 (2002). © 2002, Springer-Verlag.

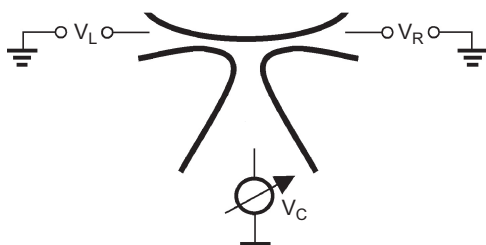
nanomaterial via coplanar probes. The experiment was performed at room temperature. Similar results were obtained in other materials with different structural parameters.

Because of the experimental limitations, the material has not been tested at frequencies higher than 50 GHz. However, from the working principle, it is expected that the cutoff frequency will be much higher, possibly up to hundreds of gigahertz or even in the terahertz regime. The large area, in combination with the in-plane layout of the material, enables straightforward and efficient coupling to high-frequency microwaves. Moreover, microwaves traveling along the normal direction of the nanomaterial surface yield the most efficient coupling, while the coupling has to be achieved in specific ways (including using antennas) in a conventional vertical device. From the material point of view, this is the first artificial electronic nanomaterial that has been demonstrated to operate at room temperature.

The possibility of generating the dc output out of an external noise signal applied to the artificial material was also investigated. As expected, a guided net flow of electrons along the upward direction was induced, which generated a negative direct voltage between L and U [72]. In many aspects, such a ratchet effect in the artificial nanomaterial resembles the photovoltaic effect in some natural crystals [49–56, 66]. For the artificial crystals, however, one can design (adjust) the size and shape of the symmetry-breaking elemental units, as well as the lattice constants. Such flexibility may also provide a new route in further studies of the photovoltaic effect.

4. THREE-TERMINAL BALLISTIC JUNCTION DEVICES

The ballistic rectifiers and the artificial materials discussed in Sections 2 and 3 are four-terminal structures. Very recently, similar nonlinear functionalities were also discovered in another type of ballistic electron device which contained three terminals [38–40, 48]. Figure 17 schematically shows one such device. Referred to as a three-terminal ballistic junction (TBJ), Y-branch, or T-branch switch, the devices were fabricated by electron-beam lithography and chemical etching using either modulation-doped GaAs-AlGaAs heterostructures [40] or modulation-doped



A three-terminal ballistic junction

Figure 17. Sketch of a three-terminal ballistic junction device. The three branches are marked L (left), R (right), and C (center). In the experiment, a voltage V is applied to the left (L) and right (R) terminals in a push-pull fashion: $V_L = -V$ and $V_R = +V$. The output voltage V_C is measured at the lower terminal.

InGaAs-InP quantum-well wafers [38, 39]. In Figure 17, the three branches are marked L (left), R (right), and C (center). In the experiment, a voltage V is applied to the left (L) and right (R) terminals in a push-pull fashion: $V_L = -V$ and $V_R = +V$. The output voltage V_C is measured at the lower terminal. For simplicity, here we consider a symmetric TBJ device. If the electron transport is diffusive, that is, if the device size is much larger than the electron mean-free path, one would expect $V_C = 0$, regardless of the value of the input voltage. However, this turned out to be not true if the electron transport is ballistic, and V_C was found to be always negative as long as $V \neq 0$. For small applied voltages, experiments showed that V_C was a quadratic function of the applied voltage V , which is in good agreement with the theory developed by Xu [48].

In his model, Xu applied the scattering theory, and obtained an analytical expression of the nonlinear effect. The key mechanism was identified to be the nonlinear properties of each of the three narrow constrictions or point contacts: the conductance of each point contact is a function of the applied voltage (or chemical potential difference) across it.

To illustrate this, we first take a look at an individual, ideal (so-called) saddle-point contact, which is connected to two reservoirs (numbered 1 and 2) at both ends, and is spatially separated from other point contacts. The electrostatic potential of the saddle point contact is expressed as

$$v(x, y) = v_0 - \frac{1}{2}m^*\omega_x^2x^2 + \frac{1}{2}m^*\omega_y^2y^2 \quad (19)$$

where v_0 is the electrostatic potential at the saddle, x along the channel direction, and y in the transverse direction. The transverse quantum confinement energy levels are equally spaced by $\hbar\omega_y$. If the etched device boundary is smooth, so-called the adiabatic approximation can be applied. At zero temperature, the electrons that have energies higher than $v_0 + (1/2)\hbar\omega_y$ may pass through this single point contact without being reflected, while electrons with lower energies will have a zero possibility of passing the point contact (total reflection). At zero applied bias $V = 0$, this leads to a multiple-step dependence of the total transmission coefficient $T_{1 \leftarrow 2, V=0} = T_{2 \leftarrow 1, V=0} \equiv T_{12, V=0}$ on the chemical potential μ_F , with $T_{12, V=0} = 1, 2, 3, \dots$, when μ_F is equal to or higher than $v_0 + (1/2)\hbar\omega_y$, $v_0 + (3/2)\hbar\omega_y$, $v_0 + (5/2)\hbar\omega_y$, ..., respectively. This actually results in the experimentally observed quantized conductance in a single quantum point contact [8, 9].

At a relatively high temperature where the thermal energy $k_B T$ is larger than the level spacing between the transverse quantum confinement modes, semiclassical approximations can be applied. The multiple-step dependence of the transmission coefficient on μ_F is smoothed out, and at zero bias voltage, T_0 becomes a linear function of μ_F :

$$T_{12, V=0} = \frac{\mu_F - v_0 + \frac{1}{2}\hbar\omega_y}{\hbar\omega_y} = \frac{\mu_F - v_0}{\hbar\omega_y} + \frac{1}{2} \quad (20)$$

as schematically shown in Figure 18.

Under the nonequilibrium condition (at a finite bias voltage V), the electrochemical potentials on both sides of the single point contact μ_1 and μ_2 become different, that is,

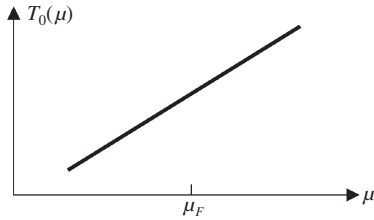


Figure 18. Linear relation between the transmission coefficients of a single, separated saddle-point contact and the chemical potential. This relation is obtained at relatively high temperatures, that is, the thermal energy $k_B T$ is larger than the level spacing between the transverse quantum confinement modes, so that the semiclassical approximation can be applied.

$\mu_1 - \mu_2 = -eV$. Because of the linear dependence of the transmission coefficient on the chemical potential, the current can be expressed as

$$I = \frac{2e}{h}(\mu_1 - \mu_2)\bar{T}_{12} = -\frac{2e^2}{h}V\bar{T}_{12} \quad (21)$$

where \bar{T}_{12} is the average transmission coefficient between μ_1 and μ_2 :

$$\bar{T}_{12} = \frac{1}{2} \left[\frac{\mu_1 + \mu_2 - 2v_0}{\hbar\omega_y} + 1 \right] \quad (22)$$

Clearly, if the applied voltage is dropped evenly on both sides of the point contact, which is a very good approximation of a single, symmetric point contact, then $\mu_1 = \mu_F - eV/2$ and $\mu_2 = \mu_F + eV/2$. Hence, such a simple model yields $\bar{T} = T_0$, and shows that the conductance is not sensitive to a change of the applied voltage. Note that this result is obtained under the conditions of a symmetric point contact, $|eV| < \mu_F$, and being at a relatively high temperature such that the thermal energy $k_B T$ is larger than or comparable to the energy spacing between the transverse quantum confinement modes. Nevertheless, the above simplified model of a single point contact can be used to reveal the mechanism of the nonlinear effect of the TBJ devices, as will be discussed later.

For a TBJ device shown in Figure 17, the situation is not as simple because these three point contacts are closely connected. Even for a symmetric TBJ, as was observed experimentally, the voltage on branch C is not the average of the voltages applied to the left and right branches (which is zero in the push-pull fashion), indicating that the voltage drop in the whole device is neither even nor symmetric. Since a self-consistent calculation on the voltage drop in such an open system is very complex to perform, for simplicity, one may assume that the applied voltage is evenly dropped at the left and right terminals: $\mu_L = \mu_F + eV$, $\mu_R = \mu_F - eV$. Here, as was in the experiments, a push-pull bias fashion is assumed, and the total applied voltage is $\mu_L - \mu_R = 2eV$. Also, for simplicity, the potential at the saddle v_0 is assumed to be zero in all of these three point contacts, which is a good approximation if the channels are not very narrow.

If the terminal on the right is positively biased and the terminal on the left is negatively biased, that is, $V_L = -V$ and $V_R = +V$ (define such a bias polarity as $V > 0$), the net

electron flows into the branch C are all from the terminal L, corresponding to a current

$$I_{C \leftarrow L} = \frac{2e}{h}(\mu_L - \mu_C) \left[\frac{\mu_L + \mu_C}{2\hbar\omega_{y(C, L)}} + \frac{1}{2} \right] t_{C \leftarrow L} \quad (23)$$

where $t_{C \leftarrow L}$ is the probability of the electrons transmitting from L to C. Here, $t_{C \leftarrow L}$ is assumed to be energy independent, which is a good approximation at a low applied voltage. $\hbar\omega_{y(C, L)}$ stands for the subband spacing of the transverse confinement modes in terminal L or in terminal C, of which $\hbar\omega_y$ is larger, and therefore of which the smaller number of occupied transverse confinement modes limits the current flow $I_{C \leftarrow L}$.

Because terminal C is a voltage probe, the net current flow in it is zero. Since $\mu_R < \mu_C, \mu_L$, the current by the electron flowing out of terminal C to R, $I_{R \leftarrow C}$, is equal to $I_{C \leftarrow L}$, and is given by

$$I_{R \leftarrow C} = \frac{2e^2}{h}(\mu_C - \mu_R) \left[\frac{\mu_C + \mu_R}{2\hbar\omega_{y(R, C)}} + \frac{1}{2} \right] t_{R \leftarrow C} \quad (24)$$

Similarly, here, $\hbar\omega_{y(R, C)}$ is the subband spacing of the transverse confinement modes in terminal C or terminal R, of which $\hbar\omega_y$ is larger, and therefore of which the smaller number of occupied transverse confinement modes limits the current flow I_{RC} .

The geometric symmetry of the device and the time-reversal symmetric lead to the relations $\hbar\omega_{y(C, L)} = \hbar\omega_{y(R, C)} \equiv \hbar\omega_{\max}$ and $t_{R \leftarrow C} = t_{L \leftarrow C} = t_{C \leftarrow L}$. Comparing Eqs. (23) and (24) yields very simple relations between the output voltage V_C , which is measured with respect to the electric ground, and the applied voltage:

$$V_C^2 - \frac{2\mu_F - \hbar\omega_{\max}}{e} V_C - V^2 = 0 \quad (25)$$

An analytical expression of the nonlinear effect in a symmetric TBJ device is obtained:

$$V_C = \frac{2\mu_F - \hbar\omega_{\max}}{2e} - \sqrt{\frac{(2\mu_F - \hbar\omega_{\max})^2}{4e^2} + V^2} < 0 \quad (26)$$

Similarly, it can be shown that the same result holds for $V < 0$ as shown in Figure 19. This explains the experimental discovery that the output voltage V_C is always negative. Remarkably, there are no geometric parameters of the device at all in Eq. (26) and the output voltage is only determined by the input voltage and the Fermi energy. The three-terminal ballistic junctions are therefore quite robust devices, and it is relatively easy to obtain a reproducible nonlinear behavior.

Note that, in the limit of a small applied voltage, $|V| \ll \mu_F/e$, the first term in Eq. (25) can be neglected because $|V_C| < |V| \ll \mu_F/e$. Therefore,

$$V_C = -\frac{e}{2\mu_F - \hbar\omega_{\max}} V^2 \approx -\frac{e}{2\mu_F} V^2 \quad (27)$$

by further assuming that $\mu_F \gg \hbar\omega_{\max}/2$, as derived by Xu in [48]. Equations (26) and (27) were obtained by assuming a parabolic confinement potential, Eq. (19), which is a good approximation for a narrow channel width. For

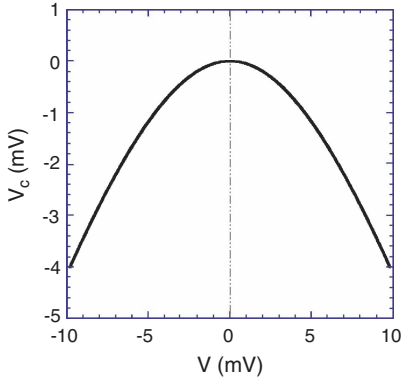


Figure 19. Theoretical results of the nonlinear output of a symmetric TBJ device. Typical parameters in the experiments were used in the calculation.

larger devices, however, a different V_c versus V relation is expected because of the different potential profiles in the device channels.

Similar to the ballistic rectifiers and nanomaterials discussed in Sections 2 and 3, TBJ devices are expected to be capable of high-frequency applications, allowed for by the ballistic transport nature and the low parasitic capacitance due to the planar device layout. This has been demonstrated in a number of experiments up to 20 GHz [73–75]. Recently, other interesting properties of the TBJ devices were predicted by Xu [76].

5. NEAR ROOM-TEMPERATURE OPERATIONS OF QUANTUM-EFFECT-BASED DEVICES

The above devices were demonstrated to function at room temperature, and the working principle is based on the semiclassical electron transport. Given the fact that the feature sizes of these room-temperature nanodevices are already comparable to the electron Fermi wavelength, it is expected to observe quantum effects not only at cryogenic, but also at elevated temperatures. In this section, we present the recent discovery of quantum effects associated with individual transverse confinement modes in some of the above devices at temperatures up to about 200 K. For the devices described in this chapter, the thermal energy $k_B T$ at room temperature is comparable to or larger than the typical energy spacing of the transverse quantum confinement modes. It is therefore difficult to observe any quantum effect that is a direct manifestation of an individual transverse energy level at room temperature. However, it is worthwhile to point out that these devices reviewed in the previous sections are, even though not directly, fundamentally based on the wave nature of the electrons: the transverse quantum confinement levels in the narrow channels or point contacts. Otherwise, in the purely classical case, N_{SD} and N_{LU} in Eq. (18) would be infinity, leading to a zero output, even if the electron transport is ballistic. For the TBJ devices, it may appear that there was no evidence of the need for quantum transport in Eqs. (26) or (27). However, the derivations of these expressions are entirely based on Eq. (20), which

actually represents the extent of the lateral quantum confinement in the point contacts. The nonlinear behavior is entirely based on the changes in the number of the occupied transverse quantum levels by the applied voltage.

Devices that display distinct quantum effects directly related to individual energy levels are expected to be ultra-fast and sensitive because of the nature of the phase coherence of the electrons. A typical example of a superconductor counterpart is the superconducting quantum interference device (SQUID). Many types of semiconductor devices that directly manifest quantum effects have been realized at low (most often liquid helium) temperatures. However, it has not yet been possible to fabricate any such quantum semiconductor device that works at room temperature, largely due to the limitation in the device fabrication.

For the ballistic rectifier shown in Figure 6 and the nanomaterial shown in Figure 15(a), evidence of quantum behavior was recently observed at temperatures up to 200 K [72]. This suggests promising possibilities of realizing and operating quantum devices at room temperature in the near future by, for example, further reducing the device size. Figure 20(a) shows the experimental result of the ballistic rectifier shown in Figure 6(a), measured at a series of temperatures. Whereas, at room temperature, the negative output voltage V_{LU} was as expected in the physical picture of semiclassical ballistic transport, rather surprisingly, V_{LU} changed sign when the temperature was lowered to about 70 K. At even lower temperatures, the device generated a pronounced oscillatory output as a function of the

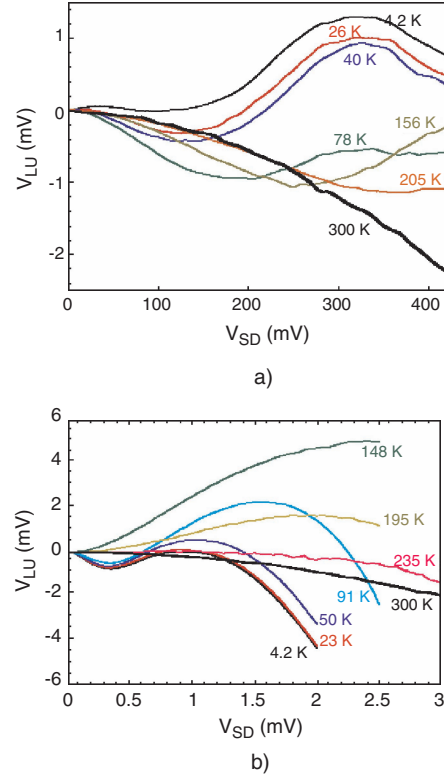


Figure 20. Normal (at room temperature) as well as reversed and oscillatory outputs (at low temperatures) of a small ballistic rectifier (a) and an artificial nanomaterial (b) as functions of the applied source-drain voltage.

applied voltage. Separate experiments showed that lower temperatures were needed to observe output reversal if the sample was illuminated by a light-emitting diode (LED) before the measurements. After the illumination, the electron concentration was increased by up to 30%, and the electron Fermi wavelength became shorter. A number of devices with different geometric parameters have also been measured, and the general trend is that, the larger the device, the lower the temperature at which the output reversal starts to be seen. Both facts suggest that quantum effects play an important role in causing the reversed and oscillatory output. This may be expected because the width of the source and drain channels, from which the ballistic electrons are ejected, is comparable to the electron Fermi wavelength (about 30–40 nm).

Recently, Fleischmann and Geisel developed a quantum model on a ballistic rectifier, and predicted reversed and oscillatory output [77–79]. The mechanism was attributed to the large difference between the channel widths of the upward and downward electron transmissions from S and D in the ballistic rectifier, that is, the gap between the triangular antidot and the edge of the upper channel is much narrower than the gap between the triangle and the edge of the lower channel. They argued that, when the applied voltage is small, the number of occupied modes of transverse quantum confinement in the (lower) wider gap may increase because of the applied voltage, while the number of occupied modes in the (upper) narrower gap remains constant due to the larger energy separation of the lateral confinement energy levels. This gives rise to the “normal” rectifying effect ($V_{LU} < 0$). If the applied voltage is high enough to open up a new mode in the upper gap, however, it was predicted that the output V_{LU} should undergo a change of sign, that is, output reversal.

While the result predicted by the model appeared to be in good agreement with the experimental data in Figure 20(a), such a mechanism for the output reversal does not seem to exist in the nanomaterials shown in Figure 15(a). This is because, in the nanomaterial, the width of the channel, which the electrons have to pass through to transmit upward after being ejected from a narrow gap between two neighboring triangles in a vertical column, is identical to the channel width of the downward electron transmission. As a result, the changes in the occupied lateral confinement modes in the channels of both the upward transmissions and the downward transmissions, induced by the applied voltage, are essentially identical. However, when measuring the nanomaterials with various geometric parameters, very similar reversed as well as oscillatory outputs were observed, which are unexpected from the model in [77]. This indicates that a different physical process is responsible for the observed oscillatory and reversed output.

Figure 20(b) shows the low-temperature experimental results of the artificial material, the geometric parameters of which are very similar to those shown in Figure 15(a). For this particular nanomaterial, the output reversal persists at up to about 200 K. Further observations, such as the dependence on device size and the influence of illuminations on the devices at low temperatures, also strongly suggest that the phenomena are a manifestation of quantum effects.

In Figure 20(a) and (b), the output is “normal” at room temperature, which has been understood in the framework of the classical ballistic transport in Section 2.2. To understand the output reversal and the oscillatory output, it was noticed that both the width of the source and drain channels in the ballistic rectifier and the width of the gaps between neighboring triangles in a vertical column in the nanomaterial are comparable to the electron Fermi wavelength, which is about 35 nm in the samples. By taking into account the finite depletion depth at the etched device boundaries, the real widths of the lateral quantum confinement are even narrower than those shown in the scanning electron micrographs. If temperature is lowered from room temperature, the electron transport may hence go from classical regime to the quantum transport regime.

Consider the ballistic rectifier first. At sufficiently low temperatures, the transverse modes in the source and drain channels become well resolved. From the width of the source and drain channels, it was estimated that there were between one and four occupied modes at low temperatures. In this estimate, the depletion depth, about 10–20 nm at each edge of the etched channels, has been taken into account. Similar to the case of a quantum point contact in the adiabatic transport regime, each mode contributes to a specific angular pattern of the electron flow from S . The number of lobes (or branches) in the pattern of electron flow corresponds to the number of maximums in $|\psi|^2$ (where ψ is the electron transverse wavefunction), as a direct result of the adiabatic transport. Therefore, for the N th transverse mode, the number of lobes is N . Such branch-like patterns of electron flow were recently imaged using a low-temperature scanning probe microscope [80, 81]. For simplicity, assume that there is only one occupied mode in the source and drain channels at zero applied voltage, which corresponds to the angular pattern of the electron flow shown in Figure 21(a), but the following discussion applies to other (if not too large) numbers of initially occupied modes. If a small negative source-drain voltage is applied, the voltage-induced collimation effect leads to a narrower angular pattern of the electron flow out of S , which is similar to the case at higher temperatures shown in Figure 9(d). As a result, the downward transmissions of the electrons deflected by the triangular antidot increase, resulting in a normal negative output V_{LU} . If the applied negative voltage is decreased further, however, the right-moving electrons from S will eventually occupy the second lateral confinement mode [25]. The second mode gives rise to a two-branch angular distribution on top of the single-branch pattern of the first occupied mode. In total, there are three lobes of electron flow, as shown in Figure 21(c). The widening of the angular distribution clearly results in an increased probability (or percentage) for the electrons to transmit upward, and a reduced probability of the downward transmissions. As shown by a detailed model and analysis in [47] (see Eq. (6) and the discussions), the output of a ballistic rectifier is determined by the relative changes of the transmission coefficients $\Delta T/T$, rather than the absolute values of the changes ΔT . Therefore, the increased probability for the electrons to transmit upward and the reduced probability of the downward transmissions, which are discussed above and illustrated in Figure 21(c), will lead to an increase in V_{LU} , and may even

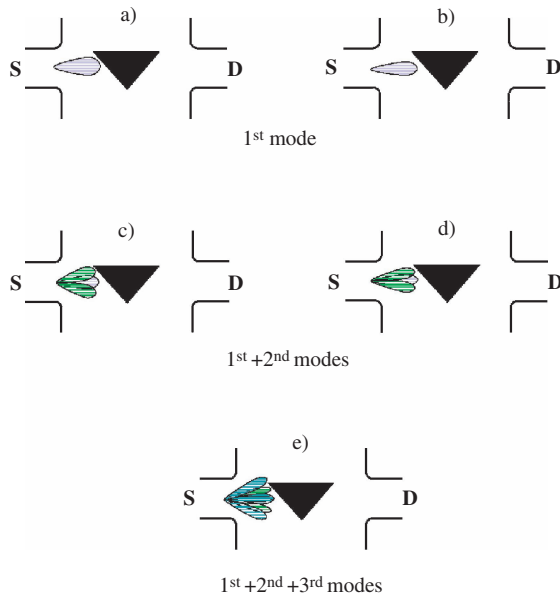


Figure 21. Schematic model for the output reversal and oscillatory output in the ballistic rectifier at low temperatures. As an example, suppose that there is only one lateral confinement mode occupied in the source channel when the applied voltage V_{SD} is zero. As a result of the adiabatic transport at low temperatures, the electrons ejected out of S have a narrow (rather than uniform) angular distribution (a). With decreasing V_{SD} , the angular distribution first becomes narrower due to the collimation effect induced by applied electric field, as shown in (b). By decreasing V_{SD} further (more negative), eventually the second lateral confinement mode becomes occupied, which gives rise to a two-branch angular distribution, on top of the single-branch pattern of electron flow of the first occupied mode. In total, there are three lobes in the electron flow (c). The total angular distribution will become narrower again with continuing decreasing V_{SD} because of the voltage-induced collimation effect (d), until at some point, the third transverse confinement mode starts to be occupied, giving rise to three additional lobes as shown in (e). Overall, by decreasing the applied voltage V_{SD} from zero, the angular distribution of the electrons ejected out of S changes alternately by subsequently narrowing (b), widening (c), narrowing (d), widening (e), and so on. Consequently, both the upward and downward transmission probabilities are oscillatory functions of V_{SD} , and this induces the oscillatory output V_{LU} which is shown in Figure 20(b).

cause output reversal (from negative to positive). If the negative applied voltage is decreased further (more negative), the applied voltage or electric field should again cause a narrowing of the overall angular pattern of the electron flow, as shown in Figure 21(d). The right-moving electrons hence have more and more chance to be scattered downward by the triangle on the right-hand side. This contributes again to a decrease in V_{LU} . A further decrease of the applied voltage will, at some point, cause the third transverse confinement mode to be occupied, giving rise to three additional lobes of electron flow, as shown in Figure 21(e), resulting in an increase in V_{LU} . Overall, by decreasing the applied voltage V_{SD} from zero, the angular distribution of the electrons ejected out of S changes alternately by subsequently narrowing (b), widening (c), narrowing (d), widening (e), and so on. Consequently, both the upward and downward transmission probabilities for the electrons ejected from S are oscillatory functions of V_{SD} , and this induces the oscillatory output.

The reversed and oscillatory output in the nanomaterial can be explained very similarly, as sketched in Figure 22. At low temperatures, similar to the case of the ballistic rectifier, by reducing the applied voltage V_{SD} from zero (more negative), the angular distribution of the electrons ejected out of each gap changes alternately by narrowing (b), widening (c), narrowing (d), widening (e), and so on, as shown in Figure 22. This similarly results in an oscillatory modulation to the transmission probabilities for the electrons to be transmitted upward and downward, and hence leads to the oscillatory output V_{LU} in the nanomaterial, as shown in Figure 20(b).

The ballistic rectifier and the nanomaterials are still much larger than the smallest devices that can be fabricated with state-of-the-art nanolithography. By, for example, reducing the device size further, it is promising that these and other new types of room-temperature quantum devices would be realized in the near future, and lead to exciting applications.

6. CONCLUSIONS AND OUTLOOK

Since the invention of the integrated circuit in 1959, the remarkable progress of the semiconductor industry has been described by Moore's law: every 12–18 months, the

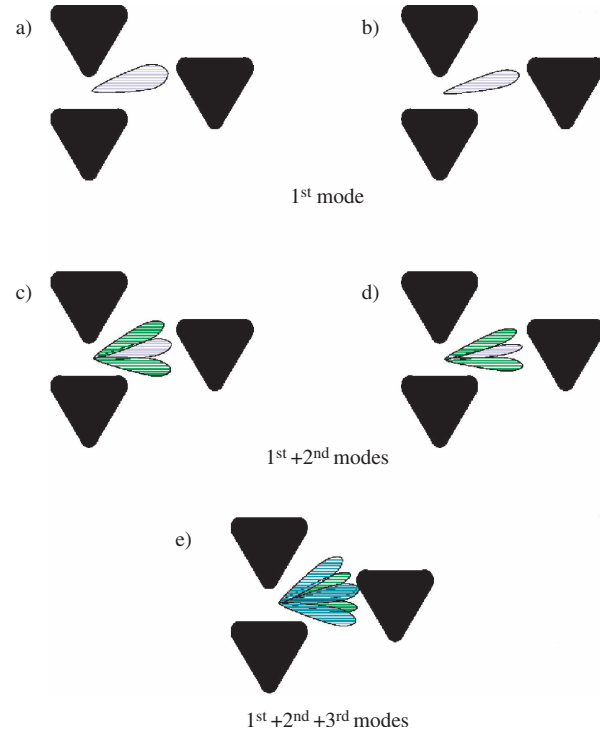


Figure 22. Schematic model for the output reversal and oscillatory output in the nanomaterial, which is similar to the case of the ballistic rectifier shown in Figure 21. For simplicity, only a small, representative part of the nanomaterial is sketched here. By decreasing the applied voltage to the nanomaterial V_{SD} from zero, the angular distribution of the electrons ejected right out of the gaps changes alternately by subsequently narrowing (b), widening (c), narrowing (d), widening (e), and so on because of the interplay between the voltage-induced collimation and the opening of additional lateral confinement modes in the gaps. As a result, the reversed and oscillatory output was observed in the experiments.

integration density of integrated circuits doubles. While such a trend has been sustained for over three decades, it has been realized for many years that the miniaturization of conventional semiconductor devices will soon reach its limit, and the following generations of electronic devices will have to be built with nanoscience and technology, and be based on completely new concepts. From an application point of view, there is substantial industrial interest in new types of nanodevices that operate at room temperature, and at gigahertz or even terahertz frequencies. Despite great efforts in explorations of novel nanodevices that can be reproducibly fabricated for mass production, and that can function at room temperature, there has been very little success. One important reason is that, in order to work at room temperature, most electronic nanodevices proposed so far require a dimension of about a few nanometers, which is at the limit of even the best state-of-the-art facilities today. For example, although the first single-electron transistor (SET) was realized more than ten years ago [82], it is still very challenging to fabricate SETs that operate at room temperature [83–85]. Apart from the operation temperature, another key issue is the working speed, which is desired to be higher than 10 GHz for the next generation of integrated circuits. A great effort has been made to design SETs that operate at high speed [86].

The investigations on novel nanoelectronic devices reviewed above have provided working devices at room temperature, as well as gigahertz frequencies. Since the required device dimensions for ballistic transport are determined by the electron mean-free path of the host material, which is fairly long (about 150 nm) in III–V heterostructures, such and other room-temperature ballistic devices can be fabricated reproducibly with the currently available techniques in the industry. Although ballistic electron transport has been studied for more than two decades, new concepts of room-temperature ballistic devices are still being discovered, such as the devices discussed in this chapter. Currently, it is still very challenging to realize ballistic electron transport in silicon materials at room temperature because of the very short mean-free path (about 10 nm) [87]. Such a precision of device fabrication is nevertheless expected to be achieved by the industry in the near future. Apart from the bottom-up approaches, such as the promising possibilities of using nanowires to build novel room-temperature devices [88, 89], the top-down approach of design and fabrication of new types of ballistic devices such as the examples introduced in this Chapter, seems to be one of the most feasible routes to provide new building blocks for the next generation of electronics.

GLOSSARY

Ballistic rectifier A new type of nanometer-scale nonlinear device that functions like a bridge rectifier. Unlike a conventional diode, the working principle is based on the ballistic electron transport and symmetry breaking, and does not require the use of a doping junction or barrier structure to achieve nonlinear functionality.

Ballistic transport A type of electron movement contrary to the diffusive transport. If the dimension of an electronic device is smaller than the electron scattering length

(mean-free path), electrons may travel from one electrode to another without encountering any scattering event from randomly distributed scatterers, such as impurities. Instead the electrons are scattered only at the device boundary, that is, moving like billiard balls. Such an electron movement is called ballistic transport.

Electron-beam lithography A standard process to create nanometer-scale structures. The resolution is generally much higher than optical lithography, well below 100 nanometers. The pattern definition is achieved by a high-energy electron beam focused on a thin layer of resist that is chemically sensitive to an electron beam. The resist layer is then developed in a suitable solution, in which either the exposed areas or the unexposed areas are selectively dissolved.

Electron mean-free path An important quantity to describe the electron transport in a material. Also often referred to as the electron scattering length, it stands for the average distance between the randomly distributed scatterers in a semiconductor material, such as defects, impurities, and phonons.

Heterostructure A multilayer semiconductor material created by growing two or more different types of semiconductors on top of each other. Each layer is normally quite thin, around tens of nanometers, and the degree of the interface homogeneity can reach the atomic level by using epitaxial growth technique, such as molecular beam epitaxy.

Mesoscopic scale The dimension between the atomic scale and macroscopic scale, typically shorter than one micron but longer than one nanometer. Ballistic electron transport devices, for instance, normally require mesoscopic dimensions.

ACKNOWLEDGMENTS

This research was supported by the Deutsche Forschungsgemeinschaft (SFB 348), the Alexander von Humboldt Foundation, the Swedish Research Councils for Engineering and Natural Sciences, the Swedish Foundation of Strategic Research, and the European Commission through LTR research project NEAR. The bulk of the experimental work described here was carried out in laboratories of Ludwig-Maximilians University München and Lund University. Writing of this review chapter was supported by UMIST. The author thanks Max Bichler, Jörg P. Kotthaus, Armin Kriele, Axel Lorke, Anneli Löfgren, Stephan Manus, Ivan Maximov, Pär Omling, Lars Samuelson, Werner Seifert, Ivan Shorubalko, Martin Streibl, Werner Wegscheider, Hongqi Xu, and Herbert Zirath for their highly appreciated contributions to the work.

REFERENCES

1. C. W. J. Beenakker and H. van Houten, in “Quantum Transport in Semiconductor Nanostructures” (H. Ehrenreich and D. Turnbull, Eds.), Solid State Physics, Vol. 44, p. 1. Academic, Boston, 1991.
2. S. Datta, “Electronic Transport in Mesoscopic Systems.” Cambridge University Press, Cambridge, 1995.
3. J. Imry, “Introduction to Mesoscopic Physics.” Oxford University Press, New York, 1997.
4. S. Ulreich and W. Zwerger, *Superlattices Microstruct.* 23, 719 (1998).

5. R. Landauer, *Philos. Mag.* 21, 863 (1970).
6. M. Büttiker, *Phys. Rev. Lett.* 57, 1761 (1986).
7. M. Büttiker, *IBM J. Res. Dev.* 32, 317 (1988).
8. B. J. van Wees, H. van Houten, C. W. J. Beenakker, J. G. Williamson, L. P. Kouwenhoven, D. van der Marel, and C. T. Foxon, *Phys. Rev. Lett.* 60, 848 (1988).
9. D. A. Wharam, T. J. Thornton, R. Newbury, M. Pepper, H. Ahmed, J. E. F. Frost, D. G. Hasko, D. C. Peacock, D. A. Ritchie, and G. A. C. Jones, *J. Phys. C, Solid State* 21, L209 (1988).
10. For a review, see, for example, R. J. Haug, *Semicond. Sci. Technol.* 8, 131 (1993).
11. M. Büttiker, *Phys. Rev. B* 38, 9375 (1988).
12. G. R. Facer, B. E. Kane, A. S. Dzurak, R. J. Heron, N. E. Lumpkin, R. G. Clark, L. N. Pfeiffer, and K. W. West, *Phys. Rev. B* 59, 4622 (1999).
13. H. van Houten, C. W. J. Beenakker, P. H. M. van Loosdrecht, T. J. Thornton, H. Ahmed, M. Pepper, C. T. Foxon, and J. J. Harris, *Phys. Rev. B* 37, 8534 (1988).
14. L. W. Molenkamp, A. A. M. Staring, C. W. J. Beenakker, R. Eppenga, C. E. Timmering, J. G. Williamson, C. J. P. M. Harmans, and C. T. Foxon, *Phys. Rev. B* 41, 1274 (1990).
15. J. Spector, H. L. Stormer, K. W. Baldwin, L. N. Pfeiffer, and K. W. West, *Appl. Phys. Lett.* 56, 1290 (1990).
16. U. Sivan, M. Heiblum, C. P. Umbach, and H. Shtrikman, *Phys. Rev. B* 41, 7937 (1990).
17. G. Timp, H. U. Baranger, P. Devegvar, J. E. Cunningham, R. E. Howard, R. Behringer, and P. M. Mankiewich, *Phys. Rev. Lett.* 60, 2081 (1988).
18. M. L. Roukes, A. Scherer, S. J. Allen, H. G. Craighead, R. M. Ruthen, E. D. Beebe, and J. P. Harbison, *Phys. Rev. Lett.* 59, 3011 (1987).
19. C. J. B. Ford, S. Washburn, M. Büttiker, C. M. Knoedler, and J. M. Hong, *Phys. Rev. Lett.* 62, 2724 (1989).
20. C. W. J. Beenakker and H. van Houten, *Phys. Rev. B* 39, 10445 (1989).
21. A. Palevski, C. P. Umbach, and M. Heiblum, *Appl. Phys. Lett.* 55, 1421 (1989).
22. C. P. Umbach, A. Palevski, M. Heiblum, and U. Sivan, *J. Vac. Sci. Technol. B* 7, 2003 (1989).
23. Y. Hirayama and S. Tarucha, *Appl. Phys. Lett.* 63, 2366 (1993).
24. K. Hieke, J. O. Wesström, E. Forsberg, and C. F. Carlström, *Semicond. Sci. Tech.* 15, 272 (2000).
25. L. P. Kouwenhoven, B. J. Vanwees, C. J. P. M. Harmans, J. G. Williamson, H. van Houten, C. W. J. Beenakker, C. T. Foxon, and J. J. Harris, *Phys. Rev. B* 39, 8040 (1989).
26. A. Palevski, C. P. Umbach, and M. Heiblum, *Appl. Phys. Lett.* 55, 1421 (1989).
27. R. Taboryski, A. K. Geim, M. Persson, and P. E. Lindelof, *Phys. Rev. B* 49, 7813 (1994).
28. R. I. Hornsey, A. M. Marsh, J. R. A. Cleaver, and H. Ahmed, *Phys. Rev. B* 51, 7010 (1995).
29. D. R. S. Cumming and J. H. Davies, *Appl. Phys. Lett.* 69, 3363 (1996).
30. A. Messica, A. Soibel, U. Meirav, A. Stern, H. Shtrikman, V. Umansky, and D. Mahalu, *Phys. Rev. Lett.* 78, 705 (1997).
31. N. K. Patel, J. T. Nicholls, L. Martin-Moreno, M. Pepper, J. E. F. Frost, D. A. Ritchie, and G. A. C. Jones, *Phys. Rev. B* 44, 13549 (1991).
32. A. Kristensen, H. Bruus, A. E. Hansen, J. B. Jensen, P. E. Lindelof, C. Marckmann, J. Nygrd, C. B. Sorensen, F. Beuscher, A. Forchel, and M. Michel, *Phys. Rev. B* 62, 10950 (2000).
33. A. Lorke, S. Wimmer, B. Jäger, J. P. Kotthaus, W. Wegscheider, and M. Bichler, *Physica B* 249–251, 312 (1998).
34. A. M. Song, A. Lorke, A. Kriele, J. P. Kotthaus, W. Wegscheider, and M. Bichler, *Phys. Rev. Lett.* 80, 3831 (1998).
35. H. Linke, W. Sheng, A. Löfgren, H. Q. Xu, P. Omling, and P. E. Lindelof, *Europhys. Lett.* 44, 341 (1998).
36. H. Linke, T. E. Humphrey, A. Löfgren, A. O. Sushkov, R. Newbury, R. P. Taylor, and P. Omling, *Science* 286, 2314 (1999).
37. H. Ueno, K. Moriyasu, Y. Wada, S. Osako, H. Kubo, N. Mori, and C. Hamaguchi, *Jpn. J. Appl. Phys.* 38, 332 (1999).
38. K. Hieke and M. Ulfward, *Phys. Rev. B* 62, 16727 (2000).
39. I. Shorubalko, H. Q. Xu, I. Maximov, P. Omling, L. Samuelson, and W. Seifert, *Appl. Phys. Lett.* 79, 1384 (2001).
40. L. Worschech, H. Q. Xu, A. Forchel, and L. Samuelson, *Appl. Phys. Lett.* 79, 3287 (2001).
41. P. F. Bagwell and T. P. Orlando, *Phys. Rev. B* 40, 1456 (1989).
42. L. I. Glazman and A. V. Khaetskii, *Europhys. Lett.* 9, 263 (1989).
43. O. Heinonen and M. D. Johnson, *Phys. Rev. Lett.* 71, 1447 (1993).
44. M. D. Johnson and O. Heinonen, *Phys. Rev. B* 51, 14421 (1995).
45. M. Büttiker, *J. Phys. Condens. Matter* 5, 9361 (1993).
46. S. Komiyama and H. Hirai, *Phys. Rev. B* 54, 2067 (1996).
47. A. M. Song, *Phys. Rev. B* 59, 9806 (1999).
48. H. Q. Xu, *Appl. Phys. Lett.* 78, 2064 (2001).
49. A. M. Glas, D. von der Linde, and T. J. Negrان, *Appl. Phys. Lett.* 25, 233 (1974).
50. V. I. Belinicher and B. I. Sturman, *Sov. Phys. Usp.* 23, 199 (1980).
51. B. I. Sturman and V. M. Fridkin, “The Photovoltaic and Photorefractive Effects in Noncentrosymmetric Materials.” Gordon and Breach, Philadelphia, 1992.
52. D. Ertaş, *Phys. Rev. Lett.* 80, 1548 (1998).
53. T. A. J. Duke and R. H. Austin, *Phys. Rev. Lett.* 80, 1552 (1998).
54. C. F. Chou, O. Bakajin, S. W. P. Turner, T. A. J. Duke, S. S. Chan, E. C. Cox, H. G. Craighead, and R. H. Austin, *Proc. Natl. Acad. Sci. USA* 96, 13762 (1999).
55. A. van Oudenaarden and S. G. Boxer, *Science* 285, 1046 (1999).
56. A. M. Song, A. Lorke, A. Kriele, J. P. Kotthaus, W. Wegscheider, and M. Bichler, “Proceedings of the 24th International Conference on Physics of Semiconductors” (D. Gershoni, Ed.), World Scientific, Singapore, 1998.
57. A. M. Song, P. Omling, L. Samuelson, W. Seifert, I. Shorubalko, and H. Zirath, *Jpn. J. Appl. Phys.* 40, L909 (2001).
58. P. Ramvall, N. Carlsson, P. Omling, L. Samuelson, W. Seifert, M. Stolze, and Q. Wang, *Appl. Phys. Lett.* 68, 1111 (1996).
59. J. Mateos, B. G. Vasallo, D. Pardo, T. González, J. S. Gallo, S. Bollaert, Y. Roalens, and A. Cappy (to be published).
60. C. W. J. Beenakker and H. van Houten, *Phys. Rev. Lett.* 63, 1857 (1989).
61. K. L. Shepard, M. L. Roukes, and B. P. Vandergaag, *Phys. Rev. Lett.* 68, 2660 (1992).
62. R. I. Hornsey, *J. Appl. Phys.* 79, 9172 (1996).
63. H. U. Baranger and A. D. Stone, *Phys. Rev. Lett.* 63, 414 (1989).
64. A. M. Song, S. Manus, M. Streibl, A. Lorke, J. P. Kotthaus, W. Wegscheider, and M. Bichler, *Superlattices Microstruct.* 25, 269 (1999).
65. A. M. Song, A. Lorke, J. P. Kotthaus, W. Wegscheider, and M. Bichler, *Superlattices Microstruct.* 25, 149 (1999).
66. H. Linke and A. M. Song, Electron ratchets—Nonlinear electron transport in semiconductor dot and antidot structures, in “Electron Transport in Quantum Dots” (J. P. Bird, Ed.), Kluwer Academic, 2003.
67. S. Y. Chou, P. R. Krauss, and P. J. Renstrom, *Science* 272, 85 (1996).
68. B. Heidari, I. Maximov, E. L. Sarwe, and L. Montelius, *J. Vac. Sci. Technol. B* 17, 2961 (1999).
69. R. Akis, D. K. Ferry, and J. P. Bird, *Phys. Rev. B* 54, 17705 (1996).
70. A. M. Song, P. Omling, L. Samuelson, W. Seifert, I. Shorubalko, and H. Zirath, *Appl. Phys. Lett.* 79, 1357 (2001).
71. A. M. Song, *Appl. Phys. A* 75, 229 (2002).
72. A. Löfgren, I. Shorubalko, P. Omling, and A. M. Song, *Phys. Rev. B* 67, 195309 (2003).
73. L. Worschech, F. Fischer, A. Forchel, M. Kamp, and H. Schweizer, *Jpn. J. Appl. Phys.* 40, L867 (2001).

74. R. Lewen, I. Maximov, I. Shorubalko, L. Samuelson, L. Thylen, and H. Q. Xu, *J. Appl. Phys.* 91, 2398 (2002).
75. I. Shorubalko, H. Q. Xu, I. Maximov, D. Nilsson, P. Omling, L. Samuelson, and W. Seifert, *IEEE Electron Device Lett.* 23, 377 (2002).
76. H. Q. Xu, *Appl. Phys. Lett.* 80, 853 (2002).
77. R. Fleischmann and T. Geisel, *Phys. Rev. Lett.* 89, 16804 (2002).
78. M. Büttiker and D. Sánchez, *Phys. Rev. Lett.* 90, 119701 (2003).
79. R. Fleischmann and T. Geisel, *Phys. Rev. Lett.* 90, 119702 (2003).
80. M. A. Topinka, B. J. LeRoy, S. E. J. Shaw, E. J. Heller, R. M. Westervelt, K. D. Maranowski, and A. C. Gossard, *Science* 289, 2323 (2000).
81. R. Crook, C. G. Smith, M. Y. Simmons, and D. A. Ritchie, *J. Phys. Cond. Matter* 12, L735 (2000).
82. T. A. Fulton and G. J. Dolan, *Phys. Rev. Lett.* 59, 109 (1987).
83. H. Ishikuro, T. Fujii, T. Saraya, G. Hashiguchi, T. Hiramoto, and T. Ikoma, *Appl. Phys. Lett.* 68, 3585 (1996).
84. L. Zhuang, L. J. Guo, and S. Y. Chou, *Appl. Phys. Lett.* 72, 1205 (1998).
85. Yu. A. Pashkin, Y. Nakamura, and J. S. Tsai, *Appl. Phys. Lett.* 76, 2256 (2000).
86. R. J. Schoelkopf, P. Wahlgren, A. A. Kozhevnikov, P. Delsing, and D. E. Prober, *Science* 280, 1238 (1998).
87. A. M. Song, M. Missous, P. Omling, A. R. Peaker, L. Samuelson, and W. Seifert, *Appl. Phys. Lett.* 83, 1881 (2003).
88. M. T. Björk, B. J. Ohlsson, T. Sass, A. I. Persson, C. Thelander, M. H. Magnusson, K. Deppert, L. R. Wallenberg, and L. Samuelson, *Nano Lett.* 2, 87 (2002).
89. M. S. Gudiksen, L. J. Lauhon, J. Wang, D. C. Smith, and C. M. Lieber, *Nature* 415, 617 (2002).